6 |

Combined solutions

6.1 Introduction

It was shown in chapter 5 that the polar gap and the coloured noise significantly contribute to a badly conditioned normal matrix. As we have seen the low orders are especially affected. Since potential coefficients up to degree and order 180 are solved for, the downward continuation does not result in any instability (compare figure 5.4). Satellite-to-satellite tracking data are reported to be less sensitive to polar gaps and may compensate for the deficient sensitivity of SGG at the longer wavelengths (Schrama, 1990). Because a GPS receiver will be mounted on the GOCE satellite high-low SST data will become available (ESA, 1999).

Besides SST other types of observations can be used to obtain better results, especially in the polar regions. To this end the combination of SGG and/or SST data with gravity data in the polar areas is studied. More specifically, a point grid of gravity anomalies at the Earth's surface is assumed to be available after the processing of airborne gravimetric data.

The outline of the chapter is as follows. The combination of SGG data with (i) SST data and (ii) gravity anomalies is considered in sections 6.3 and 6.4 respectively. This should lead to a better appreciation of the individual contribution of both data sets to the quality improvement. Section 6.5 describes the combination of all three data types. First of all, however, SGG results for different mission scenarios are described. Since in chapter 5 it is shown that the SGG simulation and error propagation results are comparable if the error model is correct, only error propagation is used from now on. Using error propagation, it is easier to study longer mission periods and to study higher maximum degrees. For reference purposes, appendix D contains results complementary to those of this chapter.

6.2 SGG results for different mission scenarios

In chapter 5 the GOCE SGG mission scenario consisted of the following constants: $N_d = 29$ days ($\approx$ 1 month), $L = 180$, $I = 96.6°$. The simulations in chapter 5 are limited to these values to keep the computations manageable. In the current chapter, however, instead of (simulated) observations, error propagation is used and higher degrees and longer missions are manageable. Now $N_d = 6$ months and $L = 180$ as well as $L = 240$ are considered.

This section and the results presented herein provide the link between chapters 5 and 6. Therefore,

Table 6.1: MSE *and bias of the different* SGG-*only solutions. The first two columns list the mission number and the mission parameters, the third column lists the α yielding the minimal* MSE. *Tikhonov regularisation with signal constraint is used in all occasions.*

mission no.	parameters	α	MSE[a]	BNR	max(BSR)[b]
1	1 m, $L = 180$, cn[c]	2.4	4.0	0.2	0.20 (117.9)
2a	6 m, $L = 180$, cn	5.1	1	0.06	0.18 (61.4)
2b	6 m, $L = 240$, cn	1.5	4.2	0.4	0.68 (2×10^3)
3	6 m, $L = 180$, wn	5.3	0.5	2.0	0.18 (386.4)

[a]In proportion to mission 2a.

[b]The maximum BSR based on the OSU91A degree-order variances. The maximum BSR between brackets has been computed using the OSU91A coefficients.

[c]The abbreviations cn and wn represent coloured noise and white noise respectively, m stands for month or months.

the GOCE SGG solution is considered first using the chapter 5 mission scenario (for the circular, inclined orbit). Then the mission length is increased from 1 month to 6 months. Although the maximum degree remains $L = 180$ for most cases, the case $L = 240$ is considered as well. At this maximum degree the error degree variances tend to equal to signal degree variances and the downward continuation starts to be more important, whereas it is not when $L = 180$ (see also the section 'Error degree variances' below). The SGG coloured noise model of chapter 5 is adopted.

Bias. Table 6.1 summarises the MSE and bias of the different SGG only solutions. Comparing missions 1 and 2a it becomes clear that α increases by a factor 2, while the number of observations increases by a factor 6 from 1 to 2a. Note that, if $N_r > 2L$ and the along track sampling is dense enough, a mission length increase of a factor 6 yields a scaling of $A^T P A$ by a factor 6. Effectively this means that mission 2a is less regularised than mission 1, although α is larger. Since more observations have been used to obtain the same number of unknowns, this is also what one would expect. The derivative of the MSE with respect to α is

$$\frac{\partial MSE}{\partial \alpha} = \sum_{i=1}^{n} \frac{2\lambda_i(\alpha \langle x, v_i \rangle - \sigma^2)}{(\lambda_i + \alpha)^3}$$

compare table 2.1 and section 2.3.3. The minimum MSE for a single i is obtained for $\alpha = \sigma^2 / \langle x, v_i \rangle$. Therefore, if the number of observations increases, σ^2 decreases and α decreases.

Mission 3 has the same mission parameters as mission 2a except for the coloured noise. The regularisation parameter $\alpha = 5.3$ seems to be only slightly larger than $\alpha = 5.1$ for mission 2a. However, the unknowns will have a smaller propagated error Q_x because of the white noise observations of mission 3. Since αK, which is proportional to the bias, is about equal for 2a and 3, the BNR will be larger for mission 3 compared to 2a, see below.

Mission 2b is the final SGG only mission discussed. Gravitational potential coefficients up to degree and order $L = 240$ are solved for, which is roughly twice the number of coefficients when $L = 180$. It is somewhat difficult to compare the normal matrix and the regularisation of mission 2b with the other missions since everything changes. Since the number of unknowns increases by roughly a factor 2 going from $L = 180$ to $L = 240$, one could say that half of the observations have been used for 2b to solve up to degree 180 compared to mission 2a, while the regularisation of 2b is about a third of the mission 2a regularisation ($\alpha = 1.5$ and $\alpha = 5.1$ respectively). The regularisation, therefore, is somewhat less for mission 2b for the degrees up to 180. Compare also figure 6.1 where the bias variance per degree and order is plotted for missions 2a and 2b. The order variance is a summation over l, and the bias order

variance of 2b is less than the bias order variance of 2a for most orders. Hence, the degrees up to 180 are less regularised in the 2b solution, which is in agreement with the smaller regularisation for 2b.

The fourth column of table 6.1 lists the MSE, that is, the trace of the MSEM, with respect to mission 2a. From a pure least-squares solution one would expect an error decrease from 1 to 2a of a factor 6 ($\sqrt{6}$ for the standard deviation). Clearly, the MSE decrease is smaller here, which must be due to the regularisation and the bias in the solution. The effect of the coloured noise on the MSE is large: the MSE for the white noise case is half of that of the coloured noise case. Also the increase of the maximum degree has a profound effect. While the number of unknowns nearly doubles, the MSE of mission 2b is more than four times larger than the MSE of mission 2a. Specifically, the downward continuation starts to play its role, amplifying noise, and the effect of the polar gap is more pronounced (compare figure 5.4).

The bias-to-noise ratio (BNR) is shown in column 5. With respect to the noise, the bias can be neglected for mission 2a, whereas the bias is not negligible for the other missions. In mission 2b, for example, the bias is a third $(0.4/(1+0.4) \approx 0.3)$ of the total error (see also appendix D, figure D.5). The large bias for the SGG white noise case can be explained by the small noise component, as stated above.

Figures 6.2 and 6.3 display the bias-to-signal ratio (BSR) for missions 1, 2a and 2b. The scales of all figures is fixed between 10^{-4} and 10^{0} in order to make the comparison easier (note that the BSR scale is logarithmic). Column 6 of table 6.1 gives the maximum of the relative bias. The maximum BSR of mission 1 between brackets differs from table 5.2 since OSU91A is used as signal here, whereas in table 5.2 the solved coefficients have been used.

If more observations are available the bias is reduced. Figure 6.2, left, is for 1 month of observations and 6.2, right, is for 6 months of observations. This is in agreement with the findings above. The relative bias is the largest for the low order coefficients, being the coefficients affected by the polar gap. Furthermore, all high degree coefficients are biased more than the lower degrees, which is caused by the regularisation ($10^{10}l^{4}$), the size of the coefficients and the downward continuation. The bias reduction due to the increase of the number of observations is restricted to the coefficients not affected by the polar gap. The effect of the polar gap becomes more evident if one solves up to degree and order $L = 240$, figure 6.3, right. Moreover, the bias increases for increasing degree.

Figure 6.3, left, displays the bias of the SGG white noise solution with respect to the SGG coloured noise solution. It is evident that the sectorial and neighbouring coefficients experience the coloured noise (see also section 5.4). The BSR itself of mission 3 is shown in figure D.1.

Error degree variances. In figure 6.4 the error degree variances of missions 1, 2a, 2b and 3 are displayed. The signal degree variances and error degree variances of OSU91A have been depicted for reference as well. For all SGG only missions it holds that the low degrees have large degree variance, especially for the coloured noise cases. The error degree variance is the smallest for the medium wavelengths and increases for the higher degrees. The white noise case and coloured noise case show large differences up to degree 30, and tend to be equal from there on. Thus, the coloured noise cause the error degree variances for low degrees to be large. At degree 240 the signal is still larger than the noise, but the degree for which the SNR becomes 1 will not be much higher.

Propagated errors. The propagation of the MSEM to geoid heights and gravity anomalies yields estimates of their uncertainties or errors and the correlations. The MSEM has a block-diagonal structure, where the $\bar{C}_{lm}$ part equals the $\bar{S}_{lm}$ part and even and odd degrees are separated. The propagated errors, therefore, are rotational symmetric and symmetric with respect to the equator. Due to the bias, however, these symmetries are not perfect but the differences turned out to be negligible. For this reason it is sufficient to draw just one longitude from north pole to equator, see figure 6.5. Shown are the geoid height and gravity anomaly errors.

The lack of data in the polar regions is responsible for the large errors there. The errors have a
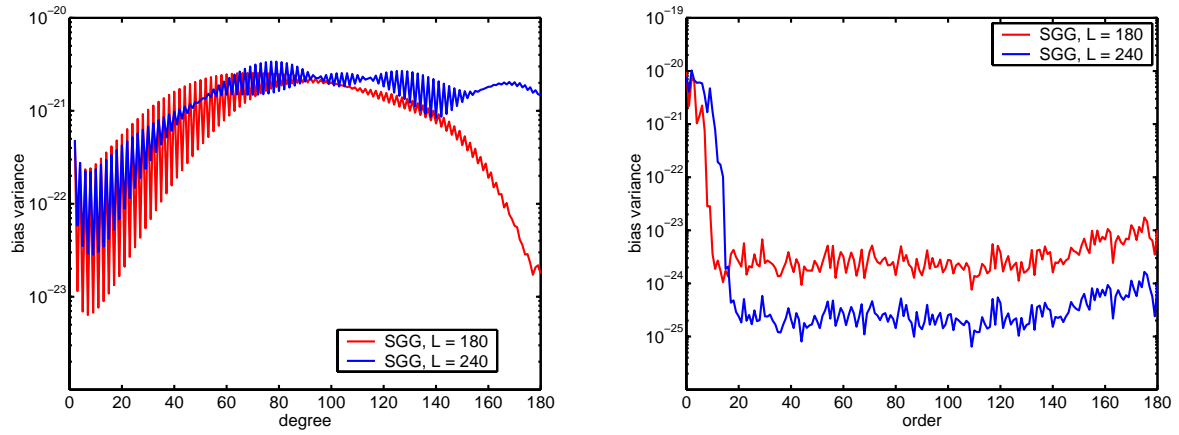
Figure 6.1: *Degree (left) and order (right) bias variances. The variances of the $L = 240$ solution were computed using terms up to degree and order 180.*
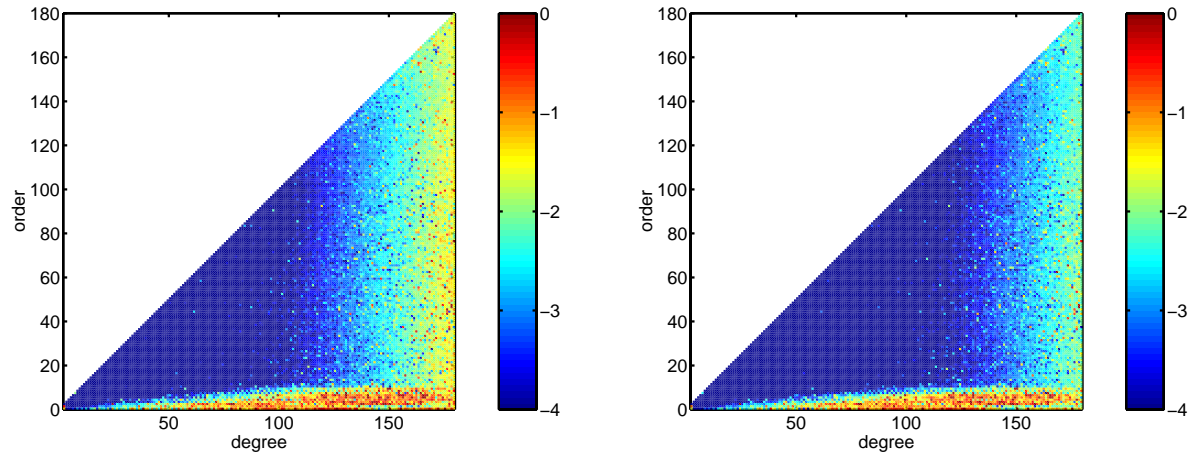

Figure 6.2: BSR*: SGG only solutions for 1 month (left) and for 6 months (right), $L = 180$. Logarithmic scale.*
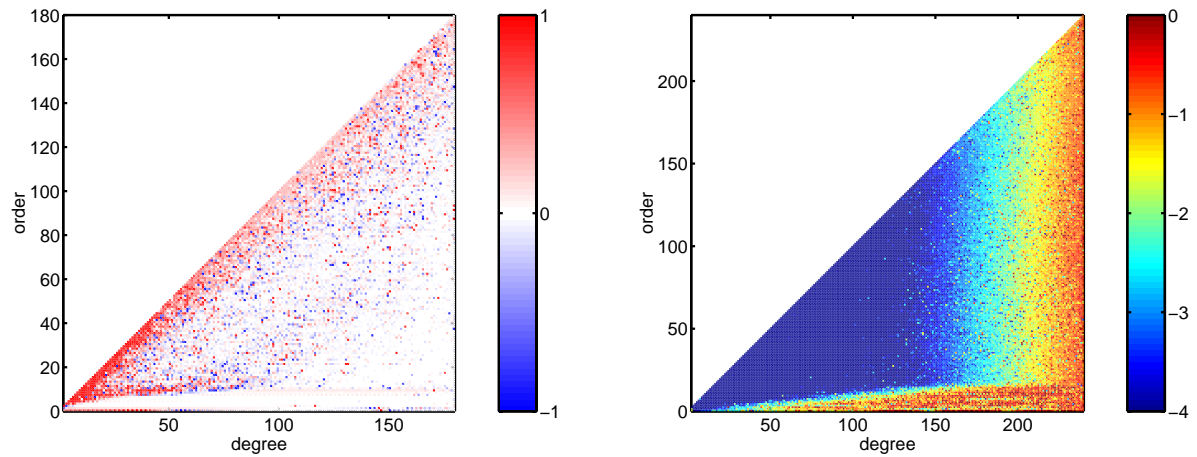

Figure 6.3: *Bias of the SGG white noise solution with respect to the SGG coloured noise solution (left).* BSR*: SGG only solution up to degree and order 240 (right). Logarithmic scale.*
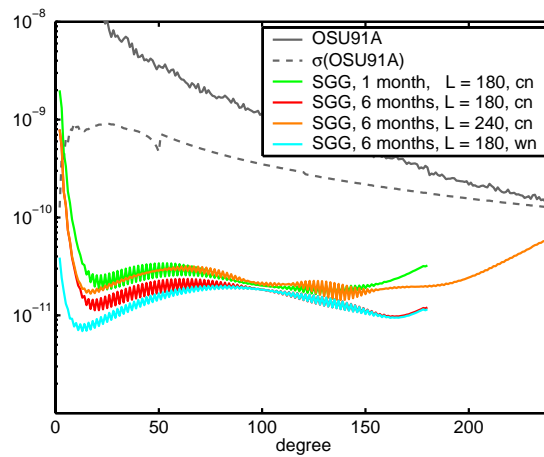
Figure 6.4: *The error degree variances for the different* SGG *mission scenarios.*
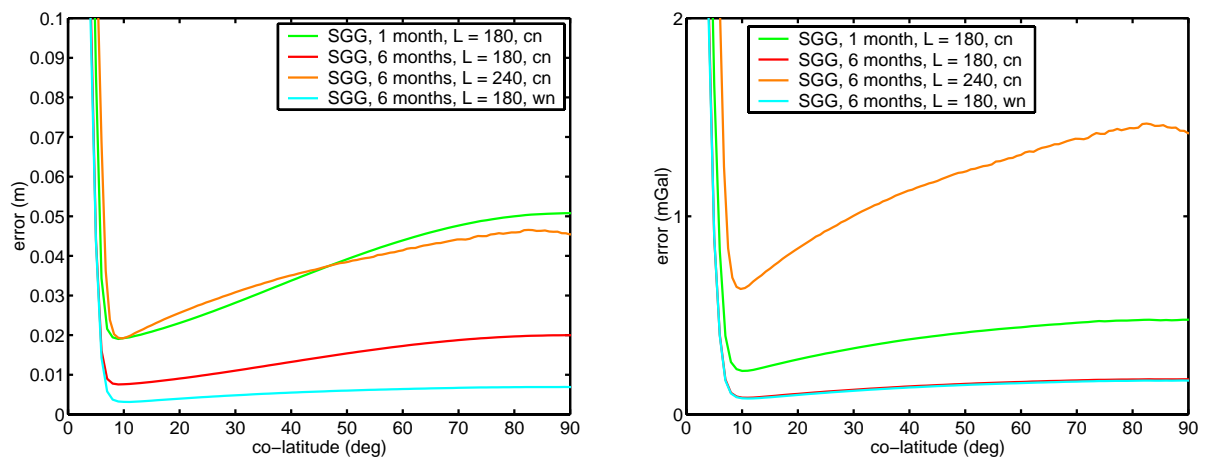

Figure 6.5: *Geoid and gravity anomaly errors according to error propagation,* SGG *measurements only. The geoid heights are on the left, the gravity anomalies on the right.*

Table 6.2: *Propagated errors for the* SGG *solutions.*

mission		geoid height error (cm)				grav. anomaly error (mGal)			
no.	parameters	RMS	mean	max	min	RMS	mean	max	min
1	1 m, $L = 180$, cn	12.3	6.1	70.8	1.9	1.48	0.71	6.98	0.22
2a	6 m, $L = 180$, cn	9.7	3.5	58.8	0.8	1.26	0.43	6.70	0.08
2b	6 m, $L = 240$, cn	11.9	6.2	54.6	1.9	2.23	1.56	10.50	0.63
2b	$l_{max} = 180$	10.8	4.1	59.8	0.9	1.55	0.57	8.66	0.13
3	6 m, $L = 180$, wn	8.3	2.4	47.1	0.3	1.18	0.41	6.73	0.08

minimum around the maximum latitude of the satellite ground track. Since there are relatively less measurements at low latitudes, the error gradually increases towards the equator. The geoid errors decrease from mission 1 to 3 (ignoring 2b). On the one hand the number of measurements increases and on the other hand the coloured noise affects the long wavelengths. Solving up to degree $L = 240$ increases the maximum geoid error in the measurement area from 2 cm to 5 cm. The anomaly error increase is much larger going from $L = 180$ to $L = 240$: 0.2 mGal becomes 1 mGal. Of course this is what could be expected since gravity anomalies are more sensitive to short wavelengths and especially the high degrees are difficult to obtain, that is, they have a relatively large uncertainty. A comparison of mission 2b ($L = 240$), truncated at $l_{max} = 180$, with mission 2a ($L = 180$) shows that the effect of the polar gap is larger for larger L: the RMS errors increase (table 6.2). Finally, it appears that the coloured noise has less effect on the gravity anomalies. The blue and red line in the right panel of figure 6.5, corresponding to white and coloured noise respectively, are almost equal. This can be explained by the smaller long wavelength sensitivity of the gravity anomalies and exactly these wavelengths are disturbed most by the coloured noise. Table 6.2 summarises the errors.

6.3   Combination of SGG and SST

Satellite-to-satellite tracking (SST) is reported to be complementary to the satellite gravity gradiometry measurements (Schrama, 1990). It is, therefore, natural to expect that the inclusion of SST observations will improve the overall quality of the gravity field solution, that is, smaller propagated errors, and bias. However, the SST normal equations are usually set up for a maximum degree of $L = 120$ (e.g. Schrama, 1990). Increasing the maximum degree for SST might increase the effect of the polar gap as is the case for SGG.

The high-low SST normal equations are set up to degree $L = 180$. In principle all these coefficients are present in the signal. As pointed out in chapter 4, a block-diagonal approach is used for the SST observations as well. This is certainly not recommended for a real life situation where one wants to obtain a gravity field model, since this approach is not good enough as shown by (Van den IJssel *et al.*, 2000). However, in this study only error propagation will be used and a block-diagonal normal matrix is supposed to give reasonable error estimates, that is, using the block-diagonal matrix one should get a fair idea of the possibilities and limitations of the SST observations. Past experience showed that a block-diagonal approach of the GEM-T1 normal matrix and a full normal matrix yield the same geoid error magnitude (Bouman, 1993). Furthermore, the SGG-SST combination results using a full error matrix can be very well compared with the results presented here (Van den IJssel *et al.*, 2000).

The error model as shown in figure 6.6 is assumed for the SST observations. The maximum errors are at 1 cpr, the along track error, x, is the largest due to the larger impact of surface forces in that direction. Since GOCE is drag compensated, the PSD may be considered as one that represents a drag compensation that is not perfect. This PSD has been derived from Topex orbit residuals (Sneeuw 1999,
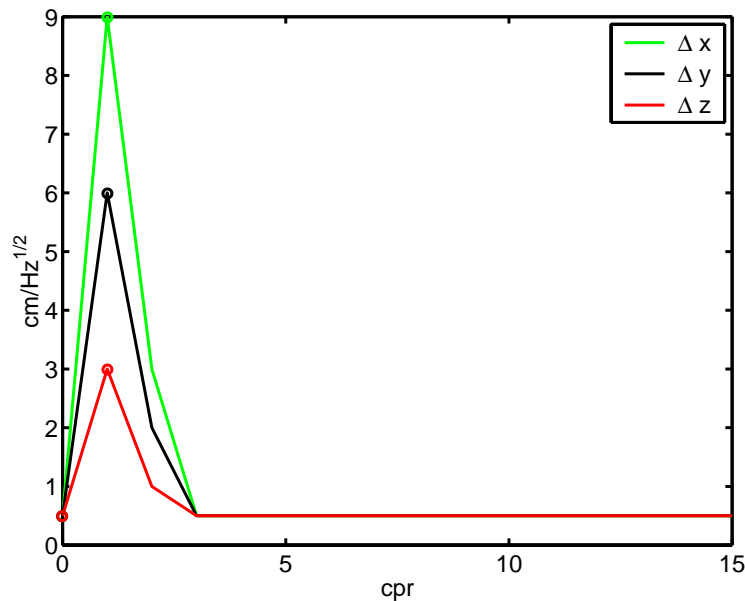
Figure 6.6: *The square root of the error* PSD *for* SST.

Table 6.3: MSE *and bias of the* SGG+SST *solutions.*

mission					
no.	parameters	α	MSE[a]	BNR	max(BSR)[b]
2a	*SGG, $L = 180$*	*5.1*	*2.9*	*0.06*	*0.18 (61.4)*
4	SGG+SST, $L = 180$	3.6	0.9	1.2	0.18 (223.0)
5a	SGG+SST/10, $L = 180$	4.3	1	1.6	0.18 (493.0)
5b	SGG+SST/10, $L = 240$	1.4	9.7	0.3	0.66 (3×10^3)
6	SGG+SST/100, $L = 180$	4.9	1.2	1.8	0.18 (539.4)

[a]In proportion to mission 5a.

[b]The maximum BSR based on the OSU91A degree-order variances. The maximum BSR between brackets has been computed using the OSU91A coefficients.

private communication). Because the error PSD is fairly optimistic above 3 cpr (Visser *et al.*, 2000), also a 10 times and 100 times more pessimistic error model are considered, denoted as SST/10 and SST/100 respectively. Most of the results in this section are presented by Bouman and Koop (1999).

Bias.   Minimisation of the trace of the MSEM yields the α values as listed in table 6.3. (Mission 2a is repeated for reference, the old values are in italic.) The less weight the SST observations get the more the value of the regularisation parameter tends to that of the SGG only value, missions no. 4, 5a and 6.

The MSE of the three SGG-SST missions 4, 5a and 6 does not change much from one mission to another. The high-low SST contributes only to the, relatively few, low degree and order coefficients. The accuracy of the SST observables is, therefore, less important. What really matters is that to the SGG observations measurements are added, sensitive to the low degrees and orders. SGG is less sensitive to those due to the nature of the measurements themselves, the coloured noise and the polar gap, see also figure 6.7.

The BNR becomes larger for smaller SST weights. Since the regularisation parameter becomes larger for smaller SST weights, while the SST weights decrease one order of magnitude each time the regularisation receives a relatively larger weight. The bias relative to the propagated error is much lower for the

Table 6.4: *Propagated errors for the combined* SGG/SST *solutions.*

mission		geoid height error (cm)				grav. anomaly error (mGal)			
no.	parameters	RMS	mean	max	min	RMS	mean	max	min
2a	SGG, *L = 180*	*9.7*	*3.5*	*58.8*	*0.8*	*1.26*	*0.43*	*6.70*	*0.08*
4	SGG+SST, $L = 180$	5.9	1.9	32.7	0.3	0.99	0.36	5.71	0.08
5a	SGG+SST/10, $L = 180$	6.5	2.0	37.2	0.3	1.06	0.38	6.02	0.08
5b	SGG+SST/10, $L = 240$	9.0	5.2	41.8	1.8	2.06	1.50	9.47	0.63
5b	$l_{max} = 180$	7.6	2.6	42.1	0.5	1.38	0.51	7.96	0.13
6	SGG+SST/100, $L = 180$	7.0	2.1	38.1	0.4	1.10	0.39	6.47	0.08

SGG only solution compared to the SGG + SST solution as a consequence of the larger propagated noise for SGG. SST doubles the number of observations and it compensates for relatively large errors due to coloured noise SGG, see 'Propagated errors' below. Since the SST/10 errors seem to be the most realistic, these weights are adopted from now on (Davis, 1997; Visser *et al.*, 2000).

The bias of the SGG only solution, missions 2a and 2b, has been compared with the SGG-SST solutions, missions 5a and 5b, see figure 6.7. Especially the coefficients affected by the coloured noise and the polar gap have more bias in the SGG only solution, while there is less bias for the low degree and order tesseral coefficients. An explanation is as follows. The bias in standard form is

$$\Delta x = -(A^T A + I)^{-1} I x$$

which means that in general the weakly determined coefficients are biased the most. If SGG and SST are combined $A^T A$ changes such that certain coefficients can be better determined and receive therefore less bias. The total bias is not only reduced but also redistributed over other coefficients (of the same order in this case) because these other coefficients gain relatively less from the additional SST measurements. Note that the biases are very small for these tesseral coefficients, see figure 6.2 and 6.3. The bias increase for these coefficients, therefore, is not as dramatic as it may appear at first sight. The BSR itself is shown in figure D.2 for the SGG + SST missions.

Error degree variances.   Figure 6.8 shows the error degree variances of the SGG-SST missions. The combined solutions outperform the SGG only solution up to degree 100 approximately. The effect of the changing SST weight is most visible in the low degrees. Since there are only a few low degree coefficients, the effect on the total MSE is not very large as shown earlier. The error degree variances of the $L = 240$ solutions are above those of the $L = 180$ solutions. Besides the fact that the same number of observations is used to estimate a higher degree solution, i.e. more unknowns, the effect of the polar gap becomes more evident. However, all propagated errors of missions 5a-b are smaller than those of missions 5a-b (table 6.2 and 6.4), see the section 'Propagated errors' below.

Propagated errors.   The propagated geoid errors are depicted in figure 6.9, left, the gravity anomaly errors in figure 6.9, right. Since the propagated errors for missions 4 and 6 resemble those of mission 5a very much, they are not shown. The combination of the SGG coloured noise measurements and the SST measurements reduces the geoid error in the measurement area to the level of the SGG only, white noise solution. SST, therefore, effectively compensates for the coloured SGG noise. This effect is, of course, negligible for the anomaly errors since the coloured noise did not have a large impact on the anomalies in the SGG only solutions. Because of the long wavelength sensitivity of SST and the high wavelength nature of gravity anomalies, the overall advantage of SST is small for the gravity anomalies. See also table 6.4 where the propagated errors have been summarised.
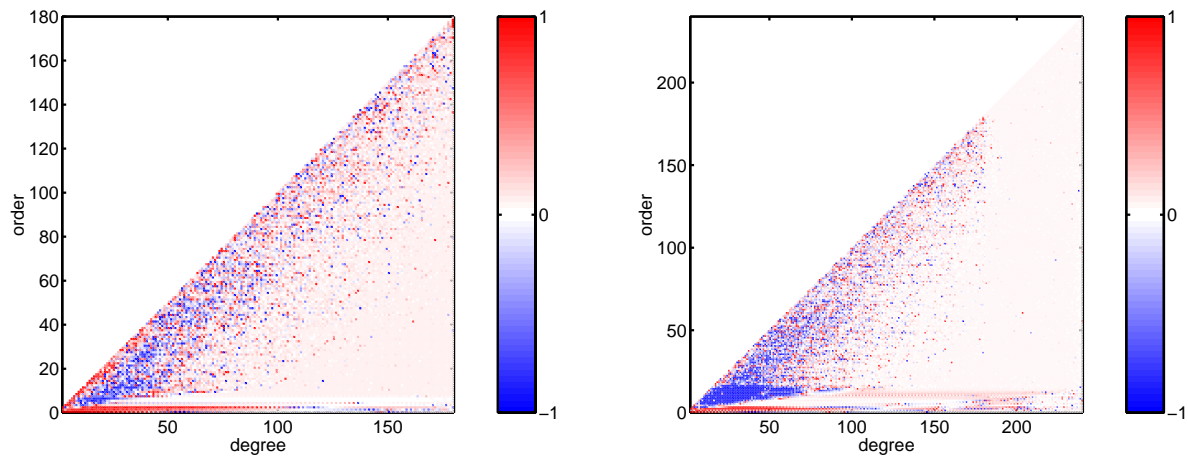
Figure 6.7: *Bias of the* SGG *solutions with respect to the* SGG+SST *solutions. Maximum degree is* $L = 180$ *(left) and* $L = 240$ *(right). Logarithmic scale.*
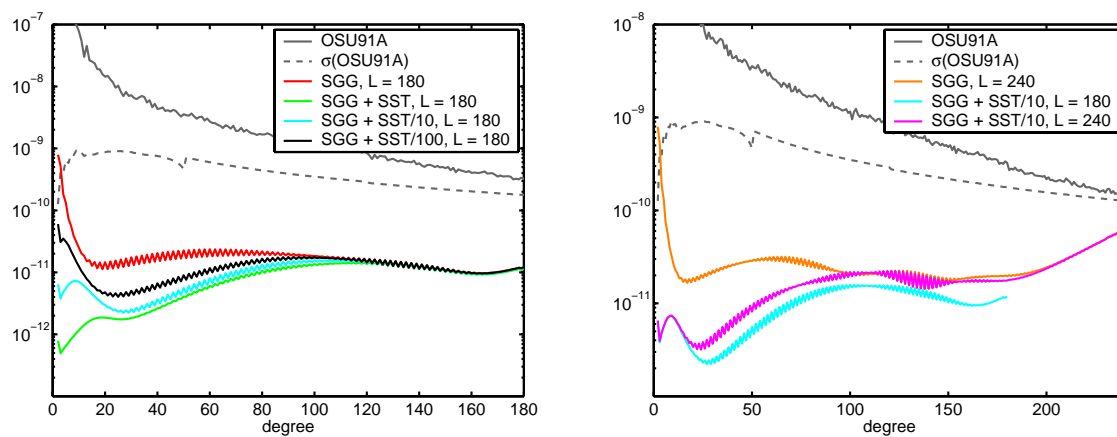

Figure 6.8: *The error degree variances for the* SGG-SST *combination. Maximum degree is* $L = 180$ *(left) and* $L = 240$ *(right).*
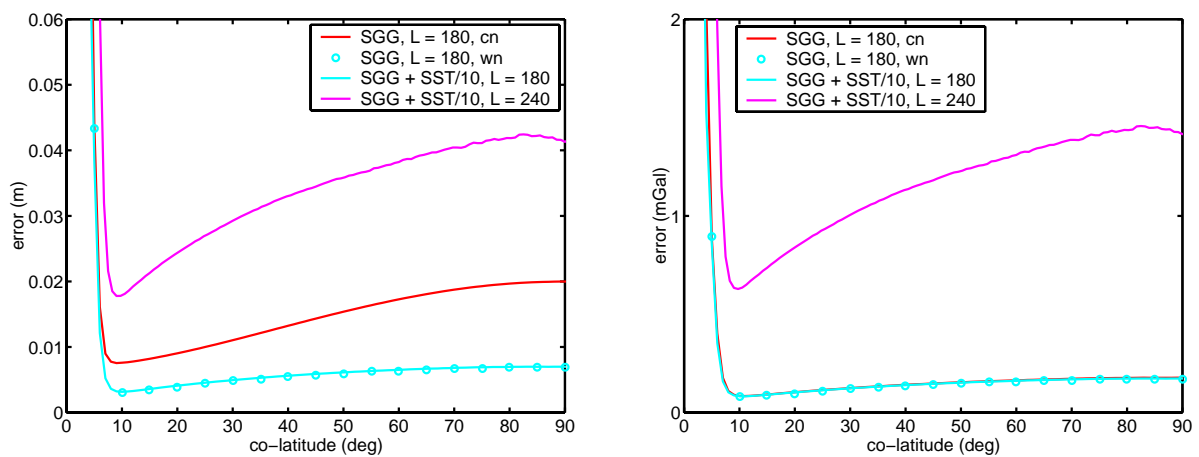

Figure 6.9: *Geoid and gravity anomaly errors according to error propagation,* SGG + SST *measurements. The geoid heights are on the left, the gravity anomalies on the right.*

Remarkably, the combination of SST and SGG reduces the geoid error in the polar area, although the polar gap still exists. The maximum geoid error is 55% - 65% compared to SGG only, table 6.4, fifth column. Effectively, the SST observations do not 'feel' the degrees above 100, see also figure 6.8. Since, for low orders, especially the high degrees have much support in the polar areas, the high degrees are affected most. Compare figure 6.10 where for $m = 0$ the Legendre functions for $l = 50, 100$ and 180 are shown. Thus the polar gap has less effect on the SGG+SST solution.

This is also supported by the increase of the minimum eigenvalues for the low orders. The right panel of figure 6.10 displays the eigenvalues of the combined SGG - SST solution with respect to those of the SGG only solution. The effect of coloured noise and polar gap have been separated. Shown are the first 12 blocks, $m = 0, \ldots, 5$, the eigenvalues are ordered increasing within each block. Comparing white noise with coloured noise and the combination with SGG alone, one may conclude that a few of the smallest eigenvalues become larger while the largest eigenvalues remain unchanged.

6.4   Combination of SGG and airborne gravimetry

The results presented in this section are an extension of the work in Bouman and Koop (1998c). There it was concluded that, to obtain geoid heights with a globally homogeneous error, two polar caps of $5°$ radius with additional gravity data suffice to constrain the solution in case of a GOCE orbit, that 5-10 mGal accuracy of the gravimetric observations is sufficient, and that larger areas with gravity anomalies hardly improve the solution because of the relatively low accuracy of the anomalies compared to the SGG measurements. However, in order to obtain a block-diagonal matrix, an equi-angular grid with a spacing of $0.125°$ has been used and white noise was assumed, the maximum degree was $L = 180$. One final result to be mentioned is that if the gravity anomalies are given in a grid with a spacing of $0.25°$ with 5 mGal anomaly accuracy, this yields the same geoid precision as gravity anomalies given in a grid with a spacing of $0.125°$ with 10 mGal anomaly accuracy.

Instead of a regular grid based on an angular scale, however, it would be more realistic to use a regular grid based on a metric scale (K. Schwarz and C. Tscherning 1998, private communication). Furthermore there is along-track correlation. Present day airborne gravimetry has an accuracy of 2-6 mGal with half wavelengths of 5-10 km as determined from cross-over points and compared to sparse upward continued data (Schwarz and Li, 1997). When cross-overs can be computed the white noise assumption is more realistic.

Based on this information the approach is as follows. It is assumed that two polar caps of $6.6°$ radius with gravity anomalies are available. The precision is 2.5 or 5 mGal for the lowest latitudes, that is for $84.4°$, but it decreases towards the pole as a function of latitude:

$$\sigma^2(\phi) = \frac{\cos \phi_0}{\cos \phi} \sigma^2(\phi_0).$$

Thus, this is equivalent to 'thinning out' the equi-angular grid towards the poles and approximates an equi-distance grid. The grid distance at $\phi_0 = 84.4°$ is 8.25 km which corresponds to $0.76°$. The decrease of this distance in km, behaving like $\cos \phi$, is compensated by the weight decrease. This approach is motivated by the earlier findings that a weight decrease of a factor 2 and a grid spacing increase of a factor 2 have exactly the same effect (Bouman and Koop, 1998c). In summary: although an equi-angular grid has been used, preserving the block-diagonal structure, the weight decrease towards the poles effectively compensates for the point density increase. Solving up to degree 240 a smaller grid size has to be chosen to fulfil the condition of chapter 4, $L < N$, with L the maximum degree of the spherical harmonic expansion and N the number of points in longitude direction. In this case the grid distance at $\phi_0 = 84.4°$ is 7.25 km which corresponds to $0.67°$.

Instead of the airborne gravimetric observations themselves, a grid of anomalies, at the Earth's surface, is used. As with the SST normal equations, quality assessment using a block-diagonal normal matrix should give a fair idea of the possibilities and limitations of the gravity anomaly measurements.

Table 6.5: MSE *and bias of the* SGG+Δg *solutions.*

mission					
no.	parameters	α	MSE[a]	BNR	max(BSR)[b]
2a	*SGG, L = 180*	*5.1*	*2.9*	*0.06*	*0.18 (61.4)*
5a	*SGG+SST/10, L = 180*	*4.3*	*1*	*1.6*	*0.18 (493.0)*
7a	SGG+Δg, $L = 180$	0.8	1.5	10^{-4}	0.00 (5.7)
7b	SGG+Δg, $L = 240$	1.2	8.5	0.07	0.55 (121.7)
8	SGG+Δg,[c] $L = 180$	1.2	1.5	3×10^{-4}	0.01 (25.1)

[a]In proportion to mission 5a.

[b]The maximum BSR based on the OSU91A degree-order variances. The maximum BSR between brackets has been computed using the OSU91A coefficients.

[c]The standard deviation of the gravity anomalies is $\sigma = 2.5$ mGal except for mission no. 8 with $\sigma = 5.0$ mGal.

Bias.   The optimal α's for the three SGG-Δg solutions, 7a, 7b and 8, are approximately 1, see table 6.5. The BNR as well as the BSR is very small, see figure 6.11. (The BSR of mission 8 is almost identical to that of 7a, compare appendix D, figure D.1. For the BNR see figure D.6.) Although the accuracy of the Δg observations is relatively poor, they are very important for constraining the low order coefficients. The effect that remains is the downward continuation of the satellite data when $L = 240$, figure 6.11, right.

Error degree variances.   The error degree variances are displayed in figure 6.12 left and right for the $L = 180$ and $L = 240$ solutions respectively. The error degree variances of mission 8 are almost equal to those of 7a and are shown in appendix D, figure D.3. The degrees between $l = 25$ and $l = 170$ are biased most due to the polar gap as shown earlier (figure 6.1). The error degree variances of these degrees, therefore, benefit most from the gravity anomaly measurements.

Propagated errors.   The geoid and gravity anomaly errors displayed in figures 6.13, left and right, show that the Δg observations only have a local effect in the space domain. The coloured noise effect on the geoid error from SGG only is not compensated for. This is also not to be expected since the additional measurements are not globally distributed and do not provide sufficient information for long wavelengths, for which the coloured noise is the most apparent. Interestingly, the maximum gravity anomaly error in the polar areas (as obtained from error propagation) is 0.5 mGal for mission 7a and 1.0 mGal for mission 7b, cf. figure 6.13 and table 6.6, while the precision of the local anomaly measurements is 2.5 mGal and 5.0 mGal respectively. Because of the correlation between the unknowns, the SGG precision 'leaks' to the polar regions.

Clearly, the gravity anomalies have a local effect only in the space domain, that is the polar areas, whereas they have a global effect in the frequency domain concerning bias reduction. The geoid error for the combination of SGG with the 2.5 mGal and 5.0 mGal anomalies stays below 4 cm and 8 cm respectively ($L = 180$). See figure D.4 for the propagated errors of mission 8. The SNR of missions 7a and 7b is shown in figure D.8, and the BNR in figure D.6.

6.5   Combination of SGG, SST and gravimetry

The combination of SGG with SST and gravity anomalies yields the most accurate gravity field solutions. The polar gaps are compensated by the gravity anomalies, whereas the SGG coloured noise is compensated by the SST observations. Only the combination of the three data types gives a nearly homogeneous quality. There are no excessive geoid height or gravity anomaly errors and the quality of the potential
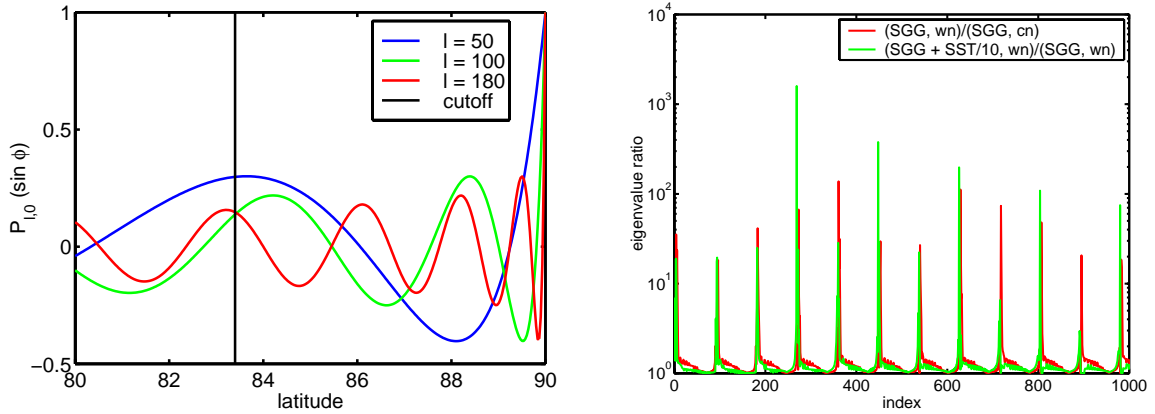
Figure 6.10: *Legendre functions for $m = 0$. The degree is $l = 50, 100$ and 180 (left panel). The eigenvalues of* SGG *with coloured noise and of* SGG + SST/10 *with respect to* SGG *with white noise (right panel). Shown are the first five orders or 12 blocks. The eigenvalues increase from left to right within each block.*
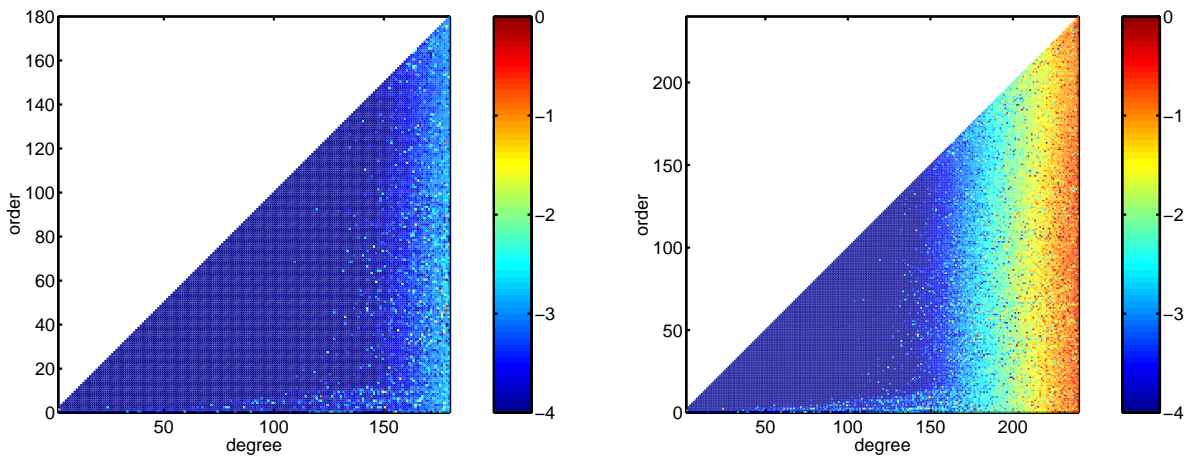

Figure 6.11: *BSR: Combination of* SGG *and* Δg, $L = 180$ *(left) and* $L = 240$ *(right). Logarithmic scale.*
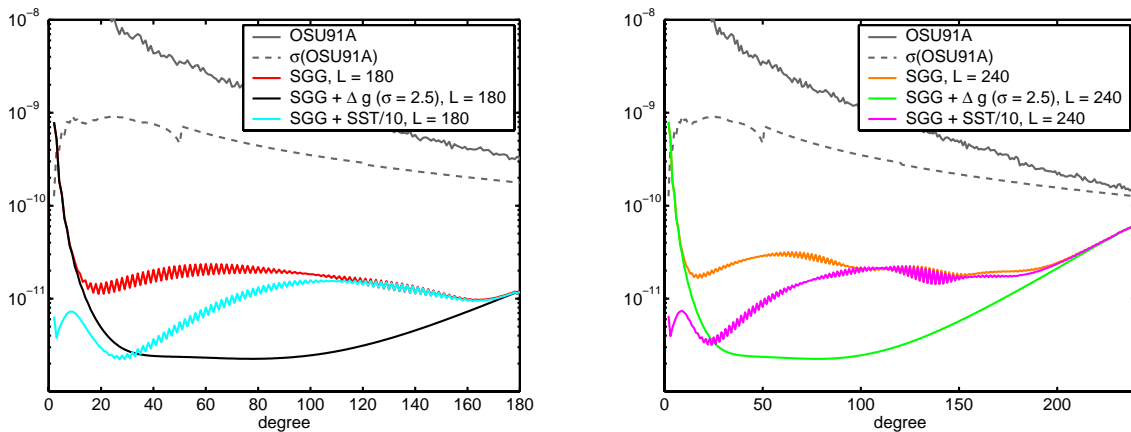

Figure 6.12: *The error degree variances for the* SGG-Δg *combination. Maximum degree is* $L = 180$ *(left) and* $L = 240$ *(right).*
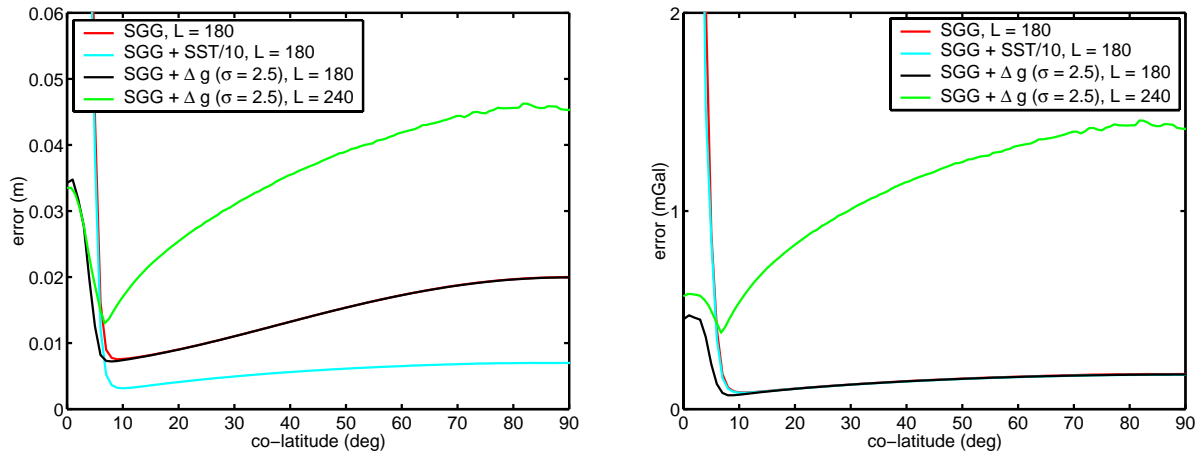
Figure 6.13: *Geoid and gravity anomaly errors according to error propagation, SGG + Δg measurements. The geoid heights are on the left, the gravity anomalies on the right.*

Table 6.6: *Propagated errors for the SGG+Δg solutions.*

mission		geoid height error (cm)				grav. anomaly error (mGal)			
no.	parameters	RMS	mean	max	min	RMS	mean	max	min
2a	SGG, *L = 180*	*9.7*	*3.5*	*58.8*	*0.8*	*1.26*	*0.43*	*6.70*	*0.08*
5a	SGG+SST/*10*, $L = 180$	*6.5*	*2.0*	*37.2*	*0.3*	*1.06*	*0.38*	*6.02*	*0.08*
7a	SGG+Δg, $L = 180$	1.7	1.5	3.9	0.7	0.18	0.16	0.53	0.07
7b	SGG+Δg, $L = 240$	3.7	3.6	4.6	1.5	1.14	1.11	1.45	0.49
7b	$l_{max} = 180$	1.6	1.5	3.1	0.7	0.17	0.16	0.42	0.08
8	SGG+Δg, $L = 180$	2.1	1.7	7.5	0.7	0.26	0.19	1.03	0.07

Table 6.7: MSE *and bias of the combined solutions.*

mission					
no.	parameters	α	MSE[a]	BNR	max(BSR)[b]
2a	SGG, *L = 180*	*5.1*	*2.9*	*0.06*	*0.18 (61.4)*
5a	SGG+SST*/10, L = 180*	*4.3*	*1*	*1.6*	*0.18 (493.0)*
7a	SGG+Δg*, L = 180*	*0.8*	*1.5*	10^{-4}	*0.00 (5.7)*
9a	SGG+SST/10+Δg, $L = 180$	0.8	0.2	6×10^{-4}	0.00 (5.6)
9b	SGG+SST/10+Δg, $L = 240$	1.2	7.3	0.09	0.55 (121.8)

[a]In proportion to mission 5a.

[b]The maximum BSR based on the OSU91A degree-order variances. The maximum BSR between brackets has been computed using the OSU91A coefficients.

Table 6.8: *Propagated errors for the combined solutions.*

mission		geoid height error (cm)				grav. anomaly error (mGal)			
no.	parameters	RMS	mean	max	min	RMS	mean	max	min
2a	SGG, *L = 180*	*9.7*	*3.5*	*58.8*	*0.8*	*1.26*	*0.43*	*6.70*	*0.08*
5a	SGG+SST*/10, L = 180*	*6.5*	*2.0*	*37.2*	*0.3*	*1.06*	*0.38*	*6.02*	*0.08*
7a	SGG+Δg*, L = 180*	*1.7*	*1.5*	*3.9*	*0.7*	*0.18*	*0.16*	*0.53*	*0.07*
9a	SGG+SST/10+Δg, $L = 180$	0.9	0.7	3.2	0.3	0.18	0.16	0.51	0.07
9b	SGG+SST/10+Δg, $L = 240$	3.4	3.3	4.2	1.4	1.14	1.11	1.45	0.49
9b	$l_{max} = 180$	0.8	0.7	2.6	0.3	0.17	0.16	0.41	0.08

coefficients is homogeneous as well. Of course, the effect of downward continuation is still present. The MSE and bias are listed in table 6.7, table 6.8 lists the statistics on the geoid height and gravity anomaly errors. Figures 6.14 and 6.15 show the error degree variances for the combined solutions and the geoid and anomaly errors according to error propagation respectively. The BSR and SNR are equal to that of the SGG-Δg combination, see appendix D (figures D.6 and D.8).

6.6 Summary

In this chapter the quality of gravity field solutions in a GOCE-like setting was investigated by means of pure error propagation. The different SGG mission scenarios show that the more measurements of the same kind are available, the smaller the bias becomes, at least for the gravity potential coefficients not affected by the polar gaps or downward continuation. Furthermore, it is shown that coloured noise of SGG observations has a large impact on the geoid errors, specifically in the area covered by observations, whereas the impact on gravity anomalies is much smaller. This is caused by the fact that the anomalies are less susceptible to long and medium wavelengths which are affected most by the coloured noise.

The SST observations reduce the bias for the coefficients affected by the coloured noise and the low order, low to middle degree coefficients affected by the polar gap. If, however, only SGG and SST observations are available, the bias cannot be neglected. While SST improves the quality of the spherical harmonic coefficients only locally (low degrees and orders) it has a global effect in the space domain on geoid errors. The improvement in the long wavelength coefficients is enough to decrease the total geoid error for the whole Earth, compensating for the SGG coloured noise.

Gravimetry in the polar areas, on the other hand, only improves the geoid error locally, that is in the polar areas. However, due to this local constraint, the quality of all low order spherical harmonic
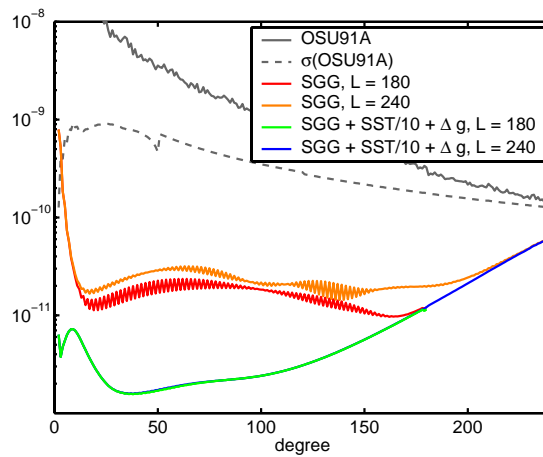
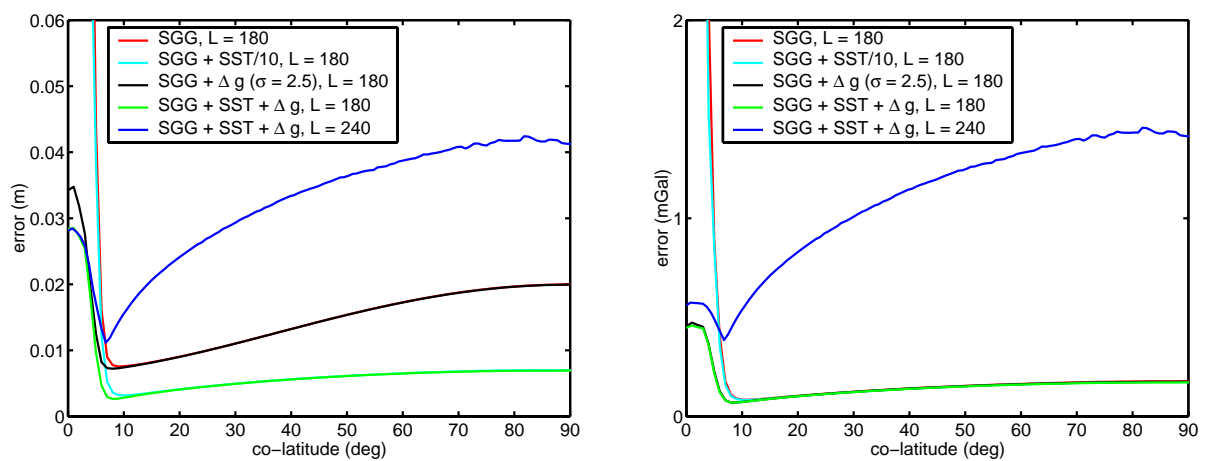Figure 6.14: *The error degree variance for the combined solutions.*

Figure 6.15: *Geoid and gravity anomaly errors according to error propagation,* SGG + SST + Δg *measurements. The geoid heights are on the left, the gravity anomalies on the right.*

coefficients improves. The gravity anomalies fully compensate for the polar gap effect, although their accuracy is low compared to the satellite observables.

To a certain extent, the accuracy of the SST and Δg measurements is unimportant. The weights of the SST observations varied between 0.5 and 50 cm/$\sqrt{\text{Hz}}$ above 3 cpr and the weights of the anomalies varied from 2.5 to 5 mGal without a large influence (note that an orbit disturbance of 10 cm corresponds to 10^{-4} E at this height). The accuracy of present day or near future state-of-the-art measurements, therefore, seems to be sufficient. The value, therefore, of the SST and Δg observations is that they enlighten a part of the function space for which the SGG observations are blind.

7 |

Conclusions and recommendations

Conclusions

The determination of a global model of the Earth's gravity field from space borne observations is an ill-conditioned inverse problem. The severeness of the ill-conditioning, due to the downward continuation and the heterogeneous data coverage, depends on the resolution of the desired model. A stable system of equations is obtained by regularisation at the expense of biased solutions. The total error of the solution can be described by the MSEM which includes propagated observation noise and bias. Of the discussed regularisation methods, the methods based on the SVD are not implemented since they involve the decomposition of the design matrix which requires too much CPU-time and memory. Tikhonov regularisation as well as biased estimation are better suited.

Although it is generally recognised that stable solutions as obtained by regularisation are biased, the solution is nevertheless interpreted in the framework of unbiased constrained least squares. A proper quality description, however, does take the bias into account. The quality assessment is based on a number of quality measures. Propagation of the MSEM to geoid height uncertainties or gravity anomaly uncertainties is of interest as well as several ratio measures such as the signal-to-noise ratio or the bias-to-noise ratio. Three contribution measures have been derived which all seem to be of little additional value in quality assessment compared to BSR for example. Of the three contribution measures, the two for biased estimators do not show the proper convergence behaviour for large regularisation parameters, that is, the contribution of the observations to the solution should go to zero but it does not. The contribution measure for unbiased estimators, applied to the biased solutions, yields large contribution values. The contribution of the observations to each spherical harmonic coefficient is more than 90%, using TR or BE up to degree $L = 180$. Nonetheless, a few coefficients suffer from large biases and propagated error which would not be expected when looking at the unbiased contribution measure.

A simulation study for SGG only, solving up to spherical harmonic degree $L = 180$ leads to the following conclusions. The polar gaps yield an extremely large condition number, 10^{10}, whereas the condition number due to downward continuation is much smaller, 10^5. However, if almost perfect observations are available, the almost exact solution is obtained even in presence of polar gaps. The circular orbit approximation may be overcome by iteration. TR with signal, first and second derivative constraint, as well as ordinary and generalised biased estimation have been used to compute a regularised solution. In the presence of polar gaps, TR with signal constraint gives the smallest mean square error of all tested

regularisation methods. The performance of TR with first derivative constraint equals that of TR with signal constraint. TR with second derivative constraint is slightly worse, specifically the high degree coefficients are more biased. Although generalised biased estimation (GBE) is designed to give the smallest MSE, it does not perform well. This is a consequence of the polar gaps which cause the low orders to be badly determined. Ordinary BE yields large errors in the polar regions, up to 20 m geoid height errors. However, in the measurement area all methods have similar performance, if the maximum degree is $L = 180$.

   The bias cannot be neglected. For the examples considered the bias is 15%-30% of the total error. The maximum BSR based on degree-order variances is 0.2-4.2, that is, the bias is maximal 20%-420% of the spherical harmonic coefficients. In the measurement area the bias can be neglected with respect to the noise for $L = 180$. The comparison of the simulated 'true' error and the error after error analysis shows that for a proper error analysis a correct noise model is a prerequisite. Notwithstanding that the normal matrix becomes block diagonal as a result of the model assumptions, the bias term of the MSEM does not. However, using only the block diagonal of the bias term is sufficient as is shown by a comparison with the simulated 'true' bias.

An error analysis for the combination of SGG with SST and/or Δg, solving up to spherical harmonic degree $L = 180$ or $L = 240$, using TR with signal constraint, leads to the following conclusions. The combination of SST and SGG yields very accurate geoid heights and gravity anomalies in the surveyed area. For a solution up to degree $L = 240$ an RMS geoid error below 5 cm and an RMS gravity anomaly error below 2 mGal, in the measurement area, seems to be realistic. Increasing the resolution from $L = 180$ to $L = 240$ means increasing the effect of the polar gap. The propagated geoid height and gravity anomaly errors increase. The effect of coloured noise on the SGG only solutions may be quite large: geoid height errors are up to a factor three larger in the measurement area, whereas gravity anomalies are nearly not affected. The coloured noise effect, however, may be fully compensated by the SST data. The added value of the latter is their sensitivity to frequencies for which SGG is less sensitive. Furthermore, SST partially overcomes the effect of the polar gaps. The bias cannot be neglected using only satellite data. Up to degree $L = 180$ the bias-to-noise ratio is between 0.06 and 2.0, that is, the bias comprises 5%-65% of the total error. The maximum bias is approximately 20% of the signal for all satellite solutions. If $L = 240$ then this maximum becomes 70%.

   For a maximum degree of $L = 180$ the combination of SGG and Δg yields geoid errors between 1 and 4 cm, and anomaly errors below 0.5 mGal. The former numbers are 0.5 cm and 3 cm for the combination of SGG, SST and Δg. If the maximum degree is $L = 240$, the geoid errors vary between 1.5 and 4.5 cm, whereas the anomaly errors are 0.5-1.5 mGal. The total power of the bias can be neglected with respect to the measurement noise if $L = 180$. Also compared to the signal the bias can be neglected. However, if $L = 240$ the maximum BSR is 55% and the bias is about 8% of the total error. The bias due to the polar gaps disappears whereas the downward continuation cannot be compensated for. In summary, assuming that the simplified error model is good enough, one can state that todays state-of-the-art airborne gravimetric data in the polar regions effectively compensate for the polar gaps, although their accuracy is relatively low compared to the satellite data. Only by these additional data a truly global high quality gravity field model is obtained.

Recommendations

The regularisation parameter has been determined by minimising the mean square error. Although this is sufficient to compare regularisation methods, it is not feasible in practice, because the true solution needs to be known. The iterative procedure towards the minimum MSE based on the least-squares solution (Xu, 1998) or its modification based on BE might be of interest in the analysis of satellite data. The exact relation of the L-curve and quasi-optimality with the MSE needs to be studied. The GCV method, which is expected to give the minimum MSE, was not implemented, because, among others, it is reported to be

sensitive to coloured noise. However, a combination of SST and SGG eliminates the effect of the coloured noise SGG error. Thus GCV might work well for a combination of these measurements.

If one is interested in a high quality gravity field model for the whole Earth, additional gravity related measurements in the polar areas to support GOCE are indispensable. To this end, a feasibility study might prove useful. Another way to improve the quality of the low order coefficients, at least for the low degrees, is to combine the GOCE solution with earlier determined gravity field models. If, however, a high quality local gravity field is needed (apart from the polar regions), then GOCE provides it.

The bias towards zero of the high degree coefficients in todays satellite-only models is generally recognised. In view of this coefficient bias, the choice of the regularisation parameter as well as the quality assessment of these models needs to be re-addressed. Since the satellite-only models serve as starting point for todays combined global gravity field models, also the combination of the satellite-only models with surface gravity data and altimetric data needs to be reconsidered. Especially bias reduction may become an important issue.

The errors in the potential coefficients studied in this thesis are either caused by measurement noise or regularisation. However, there is signal present above the maximum degree and this signal will be mapped onto the lower degrees. The precise nature and size of the errors caused by neglecting the gravitational potential coefficients above $L = 240$ need to be studied. To overcome this error, one strategy might be to solve for more coefficients than needed or suggested by the SNR. The idea is that the additional coefficients absorb most of the error. It is questionable, however, whether this is feasible. Increasing the degree means increasing the influence of the polar gap and all low order coefficients will be affected. Also the ill-conditioning due to the downward continuation increases. Moreover, the same number of measurements is used to determine more coefficients, increasing the MSE. The trade-off between a reduced effect of the neglected coefficients and the increased effect of polar gap/downward continuation and MSE deserves further attention.

Compact operators and spectral decomposition.

This appendix has been added to support chapter 2. A few definitions from functional analysis are listed and an introduction to spectral decomposition is given.

A.1   A few definitions from functional analysis

Consider the operator equation

$$Af = g$$

of the first kind. The symbol $A : F \to G$ will mean a single valued mapping whose domain of definition is F and whose range is contained in G. The *range* $R(A)$ is the set $R(A) := \{Af : f \in F\}$ of all image elements.

Injective, surjective and bijective.   If for each $g \in R(A)$ there is only one element $f \in F$ with $Af = g$ then A is said to be *injective* and its inverse mapping $A^{-1} : R(A) \to F$ is defined by $A^{-1}g := f$. The inverse mapping has domain $R(A)$ and range F. It satisfies $A^{-1}A = I$ on F and $AA^{-1} = I$ on $R(A)$ where I is the identity operator. If $R(A) = G$ then the mapping is said to be *surjective*. If it is injective and surjective the mapping is called *bijective*, that is, the inverse mapping $A^{-1} : G \to F$ exists, e.g. (Kress, 1989, p. 1).

Bounded operators.   An operator $A : F \to G$ mapping a linear space F into a linear space G is called *linear* if

$$A(c_1 f_1 + c_2 f_2) = c_1 A f_1 + c_2 A f_2$$

for all $f_1, f_2 \in F$ and all $c_1, c_2 \in \mathbb{R}$.

Definition A.1 (bounded).   A linear operator $A : F \to G$ from a normed space F into a normed space G is called *bounded* if there exists a positive number c such that

$$\|Af\|_G \le c\|f\|_F$$

for all $f \in F$. Each number c for which this inequality holds is called a *bound* for the operator A. $\square$

Definition A.2 (continuous).   Consider the mapping $A : F \to G$ where F and G are metric spaces with d the metric on G and $\tilde{d}$ the metric on F. The mapping A is said to be *stable* or *continuous* on the spaces (F, G) if for every $\varepsilon > 0$ there is a $\delta > 0$ such that

$$\tilde{d}(Af_1, Af_2) = \tilde{d}(g_1, g_2) < \varepsilon \ \ \forall f \text{ satisfying } \ d(f_1, f_2) < \delta \tag{A.1}$$

where $f_1, f_2 \in F$ and $g_1, g_2 \in G$. $\hspace{3cm}\square$

A linear operator is continuous if and only if it is bounded. Hence, for a linear operator boundedness and continuity are equivalent concepts.

Compact operators.   A linear operator $A : F \to G$ is compact if and only if for each bounded sequence $\{f_n\}$ in F the sequence $\{Af_n\}$ contains a convergent subsequence in G. Compact linear operators are bounded.

Theorem A.3.   Let F, G, H be normed spaces and let $A : F \to G$ and $B : G \to H$ be bounded linear operators. Then the product $BA : F \to H$ is compact if one of the two operators is compact. $\hspace{0.3cm}\square$

Theorem A.4.   The identity operator $I : F \to F$ is compact if and only if F has finite dimension. $\square$

Therefore, the compact operator A cannot have a bounded inverse unless its range is finite. ($A^{-1}A = I$ is not compact in infinite dimensions due to theorem A.4 and because A is compact A^{-1} has to be unbounded in view of theorem A.3.) For a proof of these theorems see (Kress, 1989, chapter 2).

A.2   Spectral decomposition

An important tool when dealing with inverse problems is the spectral decomposition of the operator. A spectrum gives clear insight in the behaviour of the operator for different frequencies and further illuminates possible ill-posedness of the problem at hand. The main references here are Lanczos (1961); Groetsch (1980); Kreyszig (1989), compare also Nashed (1976); Golub and van Loan (1996); Louis (1989); Groetsch (1993); Engl *et al.* (1996).

Definition A.5 (eigenvalues, spectrum).   Let $T : F \to G$ be a compact, symmetric (or self-adjoint, $T = T^*$) and semi-positive definite ($\langle Tf, f \rangle \geq 0 \ \forall \ f \in F$) linear operator. Then T has a finite or countably infinite number of *eigenvalues* λ_n; in the latter case $\lambda_n \to 0$ as $n \to \infty$ (the only possible point of accumulation is zero which follows from the compactness of the operator (e.g. Kreyszig, 1989, sec. 8.3)). The eigenvalues can be arranged in a sequence converging to zero

$$\lambda_1 \geq \lambda_2 \geq \cdots \geq \lambda_n \geq \cdots \geq 0 \tag{A.2}$$

with corresponding (nonzero) orthonormal eigenvectors $w_1, w_2, \cdots, w_n, \cdots$:

$$Tw_n = \lambda_n w_n.$$

The set of eigenvectors $\{w_n : \lambda_n \neq 0\}$ is a basis for $\overline{R(T)}$.[1]

The set $\sigma(T)$ of numbers λ for which the operator $T - \lambda I$ has no bounded inverse is called the *spectrum* of T. In the case of a compact, symmetric, semi-positive definite operator the spectrum is real, nonempty and every nonzero member of $\sigma(T)$ is an eigenvalue of T. The corresponding null space $N(T - \lambda I)$ is finite dimensional. $\hspace{1cm}\square$

---

[1]Since span$\{w_n\}$ is complete and $R(T)$ might not be complete. Thus the completion of $R(T)$ is needed.

The norm of T is equal to the *spectral radius*:

$$\|T\| = \max\{\lambda : \lambda \in \sigma(T)\} = \lambda_1.$$

For every $f \in F$ we may write

$$Tf = \sum_{n=1}^{\infty} \lambda_n \langle f, w_n \rangle w_n.$$

Definition A.6 (singular values, singular system).   Now consider the compact operators $A : F \to G$, $A^*A : F \to F$ and $AA^* : G \to G$. The latter two are self-adjoint and have the same nonnegative eigenvalues. If there are only nonzero eigenvalues, the spectra of both operators are the same $\sigma(A^*A) = \sigma(AA^*)$.

Denote the eigenvectors of A^*A as v_n, and the eigenvectors of AA^* as u_n. The eigenvalues, equal for both operators, are λ_n, the ordering is as in (A.2). Let $\sigma_n = \sqrt{\lambda_n}$ and $u_n = \sigma_n^{-1} A v_n$. Then

$$A v_n = \sigma_n u_n$$

and

$$A^* u_n = \sigma_n v_n.$$

The numbers σ_n are called the *singular values* for the operator A, the system $\{v_n, u_n; \sigma_n\}$ is called a *singular system* for A. □

From the last two equations above it follows that v_n and u_n are indeed eigenvectors of A^*A and AA^* respectively. The eigenvectors v_n are a complete orthonormal system or basis for

$$\overline{R(A^*)} = \overline{R(A^*A)} = N(A)^{\perp}$$

and u_n are a complete orthonormal system for

$$\overline{R(A)} = \overline{R(AA^*)} = N(A^*)^{\perp} \tag{A.3}$$

with $N(A)^{\perp}$ the space perpendicular to the null-space of A.

If and only if A has a finite-dimensional range, A has only finitely many singular values. If A is an integral operator with infinitely many singular values, they accumulate (only) at 0

$$\lim_{n \to \infty} \sigma_n = 0$$

as was the case for the eigenvalues. If there are finitely many singular values the kernel of the integral operator is *degenerate*.

The norm of A is

$$\|A\| = \sigma_1.$$

Theorem A.7 (Picard condition).   The equation of the first kind $Af = g$ has a solution if $g \in \overline{R(A)}$ and

$$\sum_{n=1}^{\infty} \sigma_n^{-2} |\langle g, u_n \rangle|^2 < \infty. \tag{A.4}$$

This is called the *Picard condition*. □

The Picard condition is a 'smoothness condition' for the right-hand side g. Since $g \in \overline{R(A)}$ one can write $g = \sum_n g_n u_n$. Because $\sigma_n^{-2} \to \infty$ for $n \to \infty$ the coefficients g_n have to decay fast enough with respect to the singular values in order to fulfil (A.4).
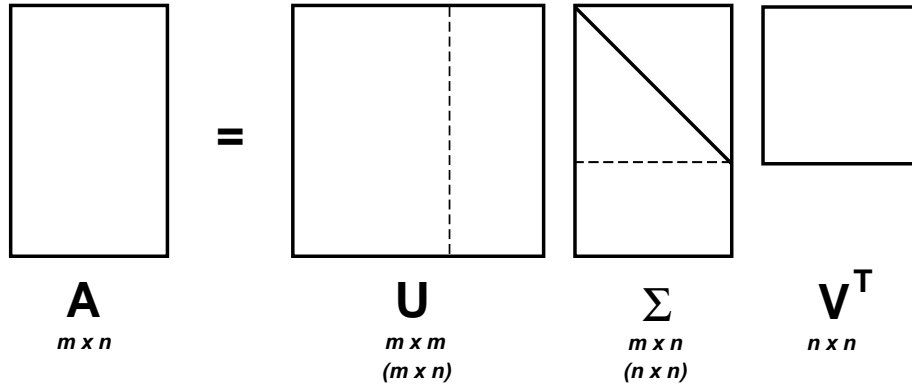
Figure A.1: *Singular value decomposition (solid lines), thin singular value decomposition (dashed lines).*

Singular value decomposition in finite dimensions.   Let $A \in \mathbb{R}^{m \times n}$, with $m \geq n$. Then the singular value decomposition of A is $A = U\Sigma V^T$ (figure A.1).

The matrices U and V are orthogonal, which means $U^T U = U U^T = I_m$ and $V^T V = V V^T = I_n$ respectively. Since the last $m - n$ rows of Σ contain only zeros, the last $m - n$ columns of U could be cancelled. This is called the thin singular value decomposition (Golub and van Loan, 1996). The resulting smaller matrix U becomes semi-orthogonal, $U^T U = I_n, U U^T \neq I_m$, compare also Lanczos (1961). The range of A is spanned by the first n columns of U, provided that all singular values are non-zero. The domain of A is spanned by the columns of V. Therefore, the large singular values denote the combination of unknowns x_i that is well represented by the measurements y. In contrast, the small singular values reveal which linear combination of unknowns are hardly recoverable from the measurements.

Generalised singular value decomposition.   The GSVD of the matrix pair (A, L) is a generalisation of the SVD of A in the sense that the generalised singular values of (A, L) are the square roots of the generalised eigenvalues of the matrix pair $(A^T A, L^T L)$ (Hansen, 1997).

Let $A \in \mathbb{R}^{m \times n}$ and $L \in \mathbb{R}^{p \times n}$ with $m \geq n \geq p$. Then the GSVD is a decomposition of A and L in the form

$$
A = U \begin{pmatrix} \Sigma & 0_{p \times n-p} \\ 0_{n-p \times p} & I_{n-p} \end{pmatrix} X^{-1}, \quad L = V \begin{pmatrix} M & 0_{p \times n-p} \end{pmatrix} X^{-1}
$$

where $U \in \mathbb{R}^{m \times n}$, $V \in \mathbb{R}^{p \times p}$ and $U^T U = I_n$, $V^T V = I_p$. $X \in \mathbb{R}^{n \times n}$ is nonsingular, and Σ and M are $p \times p$ diagonal matrices with elements:

$$
0 \leq \sigma_1 \leq \ldots \leq \sigma_p \leq 1, \quad 1 \geq \mu_1 \geq \ldots \geq \mu_p > 0
$$

which are normalised such that

$$
\Sigma^T \Sigma + M^T M = I_p.
$$

Then the *generalised singular values* γ_i of (A, L) are defined as

$$
\gamma_i = \sigma_i / \mu_i, \quad i = 1, \ldots, p
$$

and they appear in non-decreasing order (opposite to the singular value ordering for historical reasons (Hansen, 1997)).

The first p columns of $X = (x_1, \ldots, x_n)$ satisfy

$$
\mu_i^2 A^T A x_i = \sigma_i^2 L^T L x_i, \quad i = 1, \ldots, p
$$

hence $A^T A x_i = \gamma_i^2 L^T L x_i$. Thus, the x_i are called the *generalised singular vectors* of the pair (A, L). For $p < n$ the matrix $L \in \mathbb{R}^{p \times n}$ always has a nontrivial null-space $N(L)$ (Hansen, 1997). The last $n - p$ columns x_i of X satisfy

$$Lx_i = 0, \quad i = p + 1, \ldots, n$$

and they are therefore basis vectors for the null-space $N(L)$.

Relation with SVD. Only when L is the identity matrix I_n, the matrices U, Σ and V in the GSVD of (A, L) are identical to U, Σ and V of the SVD, except for the ordering of the singular values and vectors, since $p = n$, $X^{-1} = M^{-1} V^T$ and $A = U \Sigma M^{-1} V^T$. In general there is no connection between the singular values and vectors of SVD and GSVD. However, when L is well-conditioned (has a 'small' condition number, the smallest possible number is one) it can be shown that the matrix X is also well-conditioned (Hansen, 1997). The diagonal matrix Σ displays therefore, the ill-conditioning of A.

Discrete Picard condition. Hansen (1990) introduces the Picard condition for finite dimensions, since condition (A.4) is always fulfilled in finite dimensions. The unperturbed y in a discrete ill-posed problem with regularisation matrix L (see section 2.2.2) satisfies the discrete Picard condition if the Fourier coefficients $|u_i^T y|$ decay faster on the average than the generalised singular values γ. A visual inspection of a plot of the Fourier coefficients $|u_i^T y|$ and the generalised singular values γ_i could reveal the faster decay. Alternatively, one may define the ratio

$$\rho_i := \gamma_i^{-1} \left(\prod_{j=i-q}^{i+q} |u_i^T y| \right)^{1/(2q+1)} , \quad i = q + 1, \ldots, n - q$$

which is the moving geometric mean, with q a small integer (Hansen, 1990). This ratio should decay monotonically to zero.

A few remarks on local regularisation methods

Three local regularisation methods are briefly discussed. Because of the apparent shortcomings of these methods, none of them has found further consideration in this thesis.

B.1 Spherical wavelets

Spherical harmonics localise ideally in the frequency domain, that is, any spherical harmonic corresponds to a single frequency. They do not, however, show any space localisation. Better space localisation is obtained by using spherical wavelets at the expense of worse frequency localisation (see, for example, Schneider, 1997; Freeden and Schneider, 1998). Ignoring the whole theoretical background, spherical wavelets turn out to be filtered versions of the discretised integral equation relating the gradiometer values at satellite height to those at the Earth's surface. The numerical examples presented so far (ibid) use only V_{zz} in the space domain approach, assuming that the SGG measurements are contaminated with white noise and that the satellite is in a polar orbit. In this study, however, all diagonal elements of the gravity gradient tensor are of interest, as well as non-polar orbits and coloured noise. Spherical wavelets, therefore, will further not be discussed here. Concerning ordinary wavelets, refer to, for example, Blatter (1998).

B.2 Konopliv-Sjogren method

Besides the Earth's gravity field, also the Moon's (Lemoine *et al.*, 1997; Konopliv *et al.*, 1998), Mars' (Konopliv and Sjogren, 1995), and Venus' (Konopliv and Sjogren, 1996; Barriot *et al.*, 1998) fields have been modelled. Doppler tracking, from stations at the Earth, of satellites orbiting these celestial bodies enables gravity field determination. Also here, like for the Earth, the spatial distribution of the measurements is not homogeneous. Konopliv and Sjogren (1995, 1996) wish to avoid the standard regularisation technique since this biases especially the high degree coefficients to zero, yielding lower peak values in areas with large gravity signal. They therefore developed a method to partially overcome this problem accounting for the spatial distribution. The Konopliv-Sjogren method is as follows.

At the surface, the radial acceleration, a_l, from all coefficients of degree l is given by (cf. section 3.2)

$$a_l(\theta, \lambda) = -\frac{GM}{R^2}(l+1)\bar{Y}_l(\theta, \lambda).$$

The expected RMS acceleration is, using Kaula's rule (Kaula, 1966) and the orthogonality properties of the base functions,

$$(a_l)_{rms} = \frac{GM}{R^2} K \sqrt{\frac{2}{l}} \tag{B.1}$$

where K is the constant for the particular planet (or Moon). Equation (B.1) is the square root of the degree-order variance, which is

$$\frac{68.35}{\sqrt{l}} \quad \text{mGal and} \quad \frac{15}{\sqrt{l}} \text{ mGal}$$

for Mars and Venus respectively (Konopliv and Sjogren, 1995, 1996). This is the first step.

The next step is to compute an unconstrained gravity field solution ($\bar{C}_{lm}$ and $\bar{S}_{lm}$ coefficients) truncated at degree L. Sub-matrices up to degree $\ldots, l-1, l, l+1, \ldots, L$ of the total error variance-covariance matrix are propagated to acceleration uncertainties (errors) in a regular grid. The uncertainty for degree l is then given as the difference of the cumulative errors to degree l and $l-1$. For each point the degree where the acceleration error exceeds the expected acceleration signal (B.1) is called the *degree strength* D. Thus, for the degrees $D, \ldots, L$ the noise exceeds the signal.

The final step is to introduce zero values for the acceleration coming from the coefficients above the degree strength D at each point with an uncertainty approximately equal to the expected signal at the degree strength. Specifically, the acceleration at a certain point for degree strength D_i is

$$a_{D_i}(\theta_i, \lambda_i) = \frac{GM}{R^2} \sum_{l=D_i}^{L} (l+1) \sum_{m=-l}^{l} \bar{K}_{lm} \bar{Y}_{lm}(\theta_i, \lambda_i) \tag{B.2}$$

where $\bar{K}_{lm} = 0$ for $l = D_i, \ldots, L$. These 'observations' are merged with the original (linearised) observation equations

$$E\left\{\begin{pmatrix} y_1 \\ y_2 \end{pmatrix}\right\} = \begin{pmatrix} A_1 \\ A_2 \end{pmatrix} x, \quad D\left\{\begin{pmatrix} y_1 \\ y_2 \end{pmatrix}\right\} = \begin{pmatrix} P_1^{-1} & 0 \\ 0 & P_2^{-1} \end{pmatrix}$$

with the least-squares solution

$$\hat{x} = (A_1^T P_1 A_1 + A_2^T P_2 A_2)^{-1} (A_1^T P_1 y_1 + A_2^T P_2 y_2). \tag{B.3}$$

The observation vector y_1 contains the differences of the satellite tracking data and the nominal data from the nominal gravity field, while y_2 contains the differences of (B.2) computed with zero coefficients and (B.2) computed with the nominal coefficients. The weight matrix P_2 is diagonal and is approximately equal to the signal at the degree strength (10 to 20 mGal for Mars). Since actual signals at certain locations can be much larger than the Kaula rule, the a priori observations y_2 over these regions are relaxed, that is, they are either removed or their weight is decreased (Konopliv and Sjogren, 1995).

The above method has not been implemented for the following reasons:

- The least-squares solution (B.3) combines the unconstrained l.s. solution with zero observations, to which end the unconstrained l.s. solution needs to be evaluated explicitly. However, it might occur that due to numerical instability such an unconstrained solution cannot be computed.

- Konopliv and Sjogren (1995, 1996) claim that the main advantage of this spatial constraint instead of a straight Kaula rule appears to be better determination of peak amplitudes. This is true as far as the constraint is removed or relaxed. However, to do so one must know in advance the gravity signal, for example from earlier gravity field solutions, DTM's or from a first guess using observations. In any case, this is not really straightforward.

B.3   Additional constraints

In addition to the usual problem of minimising

$$J_\alpha(x) = \|Ax - y^\varepsilon\|_2^2 + \alpha\|x\|_2^2$$

it is possible to define a (linear) side constraint of the form

$$Cx \geq s \tag{B.4}$$

where C is an $l \times n$ matrix and s a known l vector. If for instance x_i is a physical parameter that should be positive then $C = I$ and $s = 0$. One could think, for example, of the light intensity of a pixel in a picture or of the distance between two points. The problem of minimising

$$J(x) = \|Ax - y^\varepsilon\|_2^2$$

the least-squares problem, with linear inequality constraint and a computation algorithm is treated by Lawson and Hanson (1974). The total system of equations becomes non-linear and Lawson and Hanson (1974) show how this can be solved iteratively. Hemmerle and Brantle (1978) discuss GBE with linear inequality constraint.

   A future application in geodesy might be gradiometric analysis. It is well known that SGG results in badly determined low order gravitational potential coefficients (Van Gelderen and Koop, 1997). This problem might partially be overcome by fixing the sign of the coefficients. One could for example adopt the sign of an existing gravitational potential model when the SNR of a specific coefficient of this model is larger than a certain threshold. This method, however, is not applied here. The side constraint as given in (B.4) is deterministic, whereas the sketched application is of stochastic nature.

Synthesis of SGG observations

C.1 Interpolation

The direct computation of the gravity gradients T_{ij} along the satellite orbit is time consuming. For each observation point (new r, ϕ and λ) a new series expansion has to be evaluated. This means that for every point one has to evaluate anew the Legendre functions and/or their derivatives together with $\cos m\lambda$ and $\sin m\lambda$. The direct computation can be avoided by pre-computing gravity gradients in regular grids at several altitudes. The values are then obtained by interpolation. If the interpolation error is one or more orders of magnitude smaller than the simulated observation error this approach is valuable and acceptable. Hereafter the computation of the observations is discussed in more detail.

The approach followed does not demand much computer time and is accurate enough, that is, the RMS interpolation error is 2 to 3 orders smaller than the measurement error as will be shown. The idea is as follows (see also figure C.1).

- Compute the actual orbit.

- Subtract GRS80 from the 'true' gravity field (for example OSU91A). This reduces the size of the signal, hence the interpolation error becomes smaller.

- Compute grids with T_{ij} in a north-east frame at four heights with FFT. The two middle grids are at the minimum and maximum height of the orbit respectively. The other two grids are below and above the orbit such that the height increment between the grids is constant (equidistant).

- Interpolate horizontally, that is, in ϕ and λ in the four grids using Overhauser splines. An Overhauser spline is a non-smooth (C^1) cubic spline, that is, it is one time continuously differentiable at the data points (see Overhauser, 1968; Klees, 1999).

- Interpolate in the vertical direction, again with Overhauser splines.

- Add the GRS80 contribution to obtain V_{ij} in the orbit points (optionally).

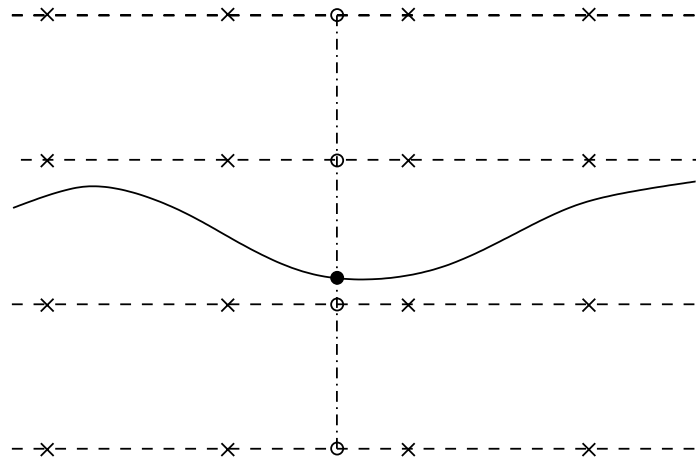- Rotate the gradients (full tensor) from the north-east frame to the local satellite frame.

Figure C.1: *Interpolation in grids, the grid points are given by* ×. *These points are used for the two-dimensional interpolation to obtain the interpolation points* ∘. *Thereafter, these points are used to interpolate in one-dimension and* • *is obtained.*

C.2   Error test

The interpolated values were compared with gradients computed by direct evaluation of the series expansion at the measurement point to test whether the interpolation error is acceptable. In total the gravity gradients in 10.000 points have been compared with a 5 second interval between them, figure C.2. The average orbit height of GOCE is 250 km, and the vertical spacing using 4 grid levels is 15 km approximately, while $\Delta\phi = \Delta\lambda = 1/8°$ which corresponds to 14 km at the equator. Both the exact and the interpolated gradients were computed in a north-east frame, using OSU91A up to degree and order 360. Since the computation of V_{xx} involves the computation of the second derivative of the Legendre functions, it is not computed directly. Instead, the harmonicity of V is exploited to compute $V_{xx} = -V_{yy} - V_{zz}$, and the Legendre functions have to be computed up to the first derivative only.

The minimum obtainable error is 10^{-7} E since the grids are stored as long integers to save disk space. A long integer has 8 bytes or 32 bits on our computer, which means that the maximum number one can store is $\pm 2^{31}$, one bit is needed for the sign. Therefore, gravity gradients up to 999 E can be stored retaining 7 significant digits after the decimal point or 10^{-7} E.

A first test with 4 grid levels in the radial direction gave an RMS difference of $\pm 10^{-5}$ E with absolute maxima of 10^{-4} E, compare figures C.3, C.4, C.5 and table C.1. Although this is well below the integrated observation noise of approximately 2×10^{-4} E, a second test was conducted with 5 grid levels instead of 4. This gave RMS differences of $\pm 10^{-6}$ E, see table C.1. The vertical spacing is the half of the previous vertical spacing and the interpolation uses the four grid levels closest to the observation point.

Since the interpolation error decrease, going from 4 to 5 grid levels, outweighs the additional effort of computing 5 levels instead of 4, it was decided to use 5 grid levels in the radial direction. The spacing in latitude and longitude direction turns out to be small enough. The interpolation error is uniform using 5 grid levels, i.e. it has the same magnitude for 3 directions.
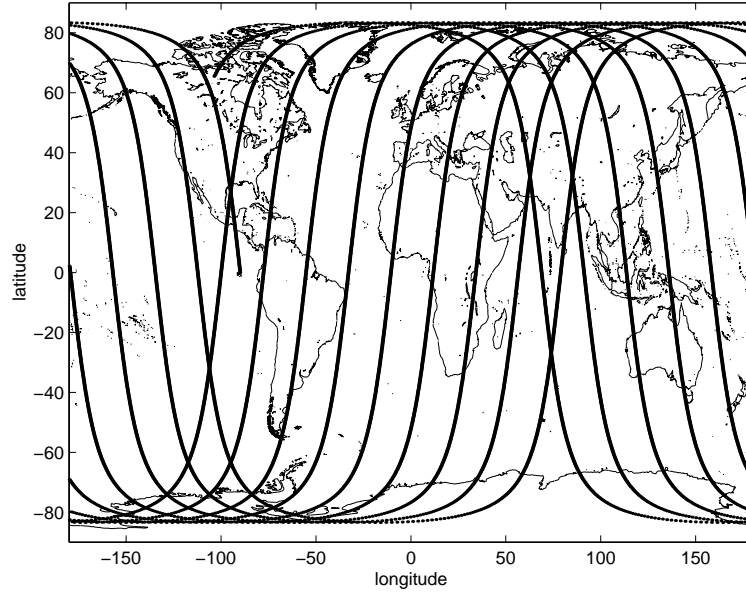
Figure C.2: *The ground tracks of the tested interpolation points.*

Table C.1: *The interpolation error for T_{xx}, T_{yy} and T_{zz} in Eötvös units ($10^{-9} s^{-2}$). The measurement noise in chapters 5 and 6 is at the 0.1 mE level.*

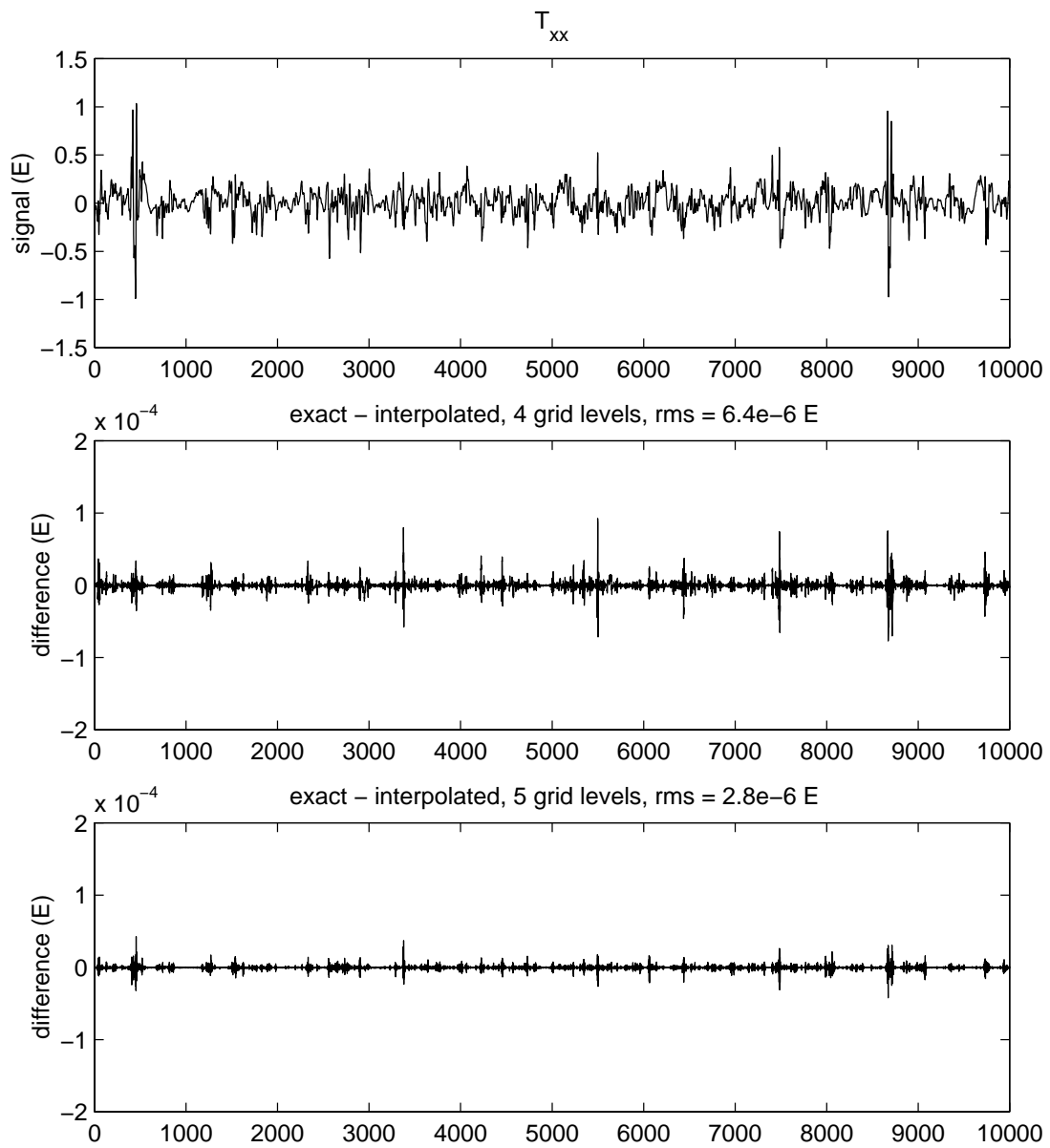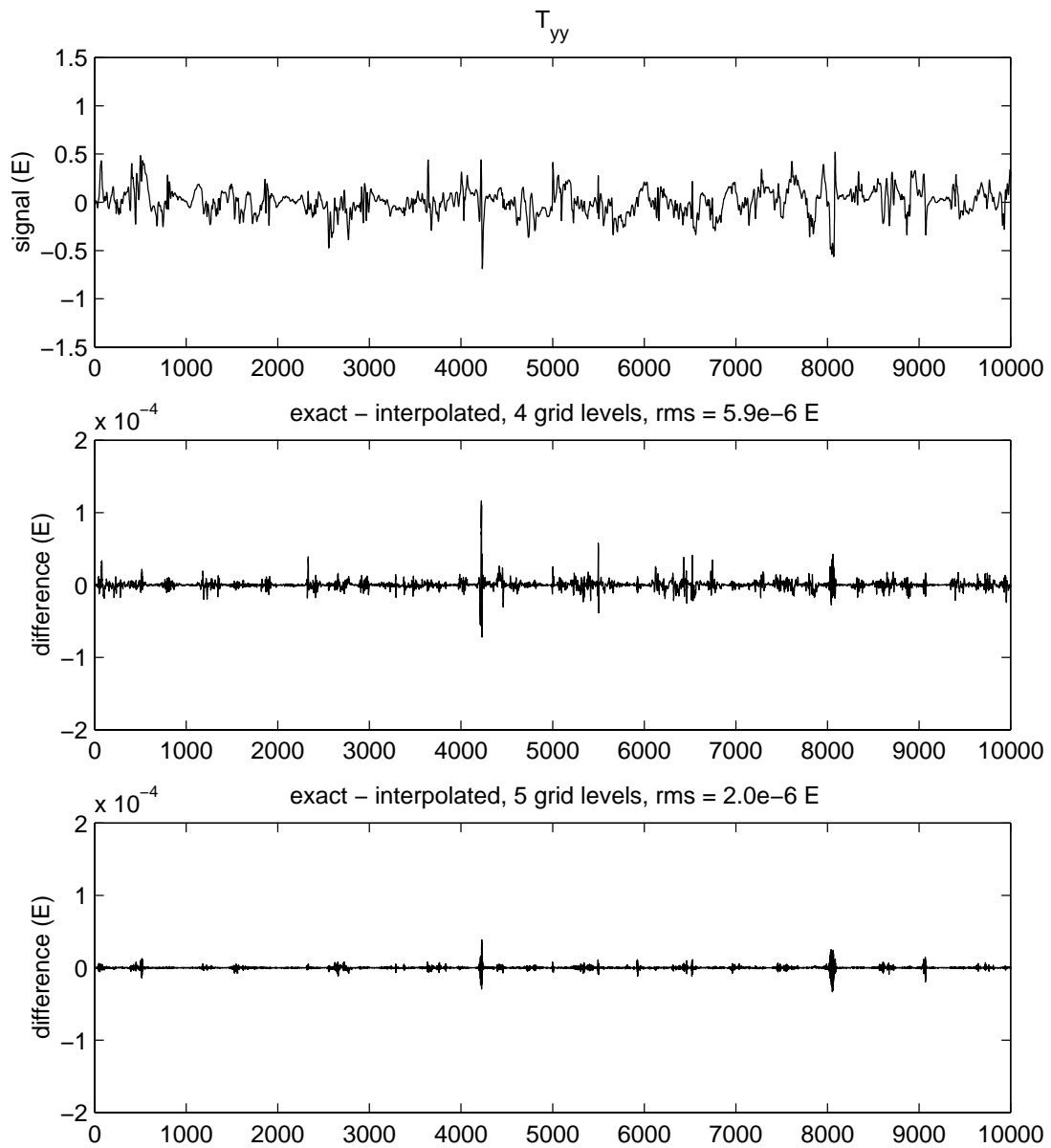|	T_{xx}		T_{yy}		T_{zz}	
	4 grids	5 grids	4 grids	5 grids	4 grids	5 grids
RMS	$6.4 \cdot 10^{-6}$	$2.8 \cdot 10^{-6}$	$5.9 \cdot 10^{-6}$	$2.0 \cdot 10^{-6}$	$1.0 \cdot 10^{-5}$	$3.9 \cdot 10^{-6}$
max	$9.3 \cdot 10^{-5}$	$4.3 \cdot 10^{-5}$	$1.2 \cdot 10^{-4}$	$3.9 \cdot 10^{-5}$	$1.5 \cdot 10^{-4}$	$5.2 \cdot 10^{-5}$
mean	$-2 \cdot 10^{-7}$	$-2 \cdot 10^{-7}$	$3 \cdot 10^{-7}$	$1 \cdot 10^{-7}$	$-1 \cdot 10^{-7}$	$1 \cdot 10^{-7}$

Figure C.3: *Signal and interpolation error for T_{xx} in a north-east frame.*

Figure C.4: *Signal and interpolation error for T_{yy} in a north-east frame.*
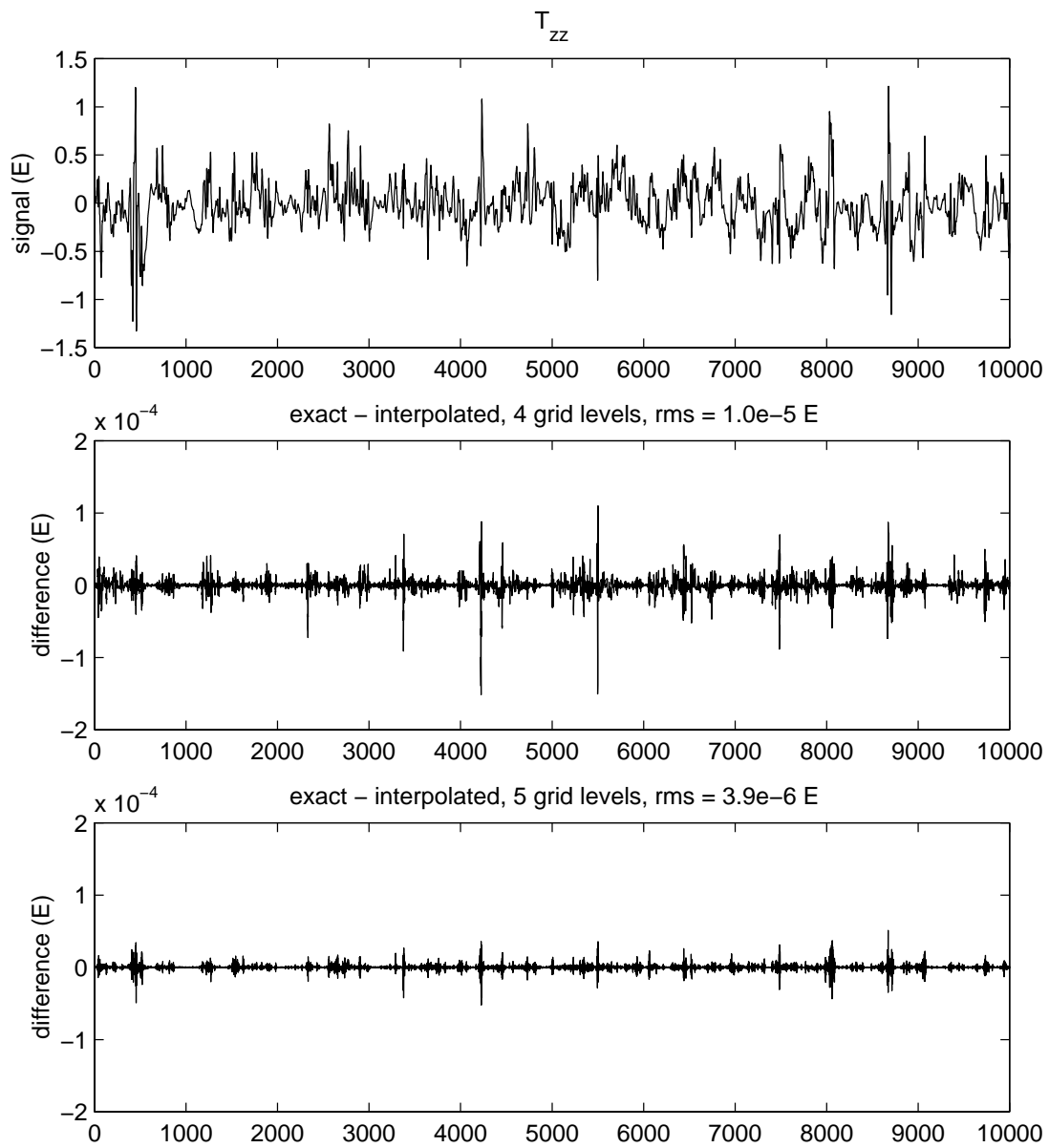
Figure C.5: *Signal and interpolation error for* T_{zz} *in a north-east frame.*

Additional results

For reference purposes results in addition to those of chapter 6 are listed here. Furthermore, a few of the results of chapter 6 are shown again, to facilitate the comparison. The tables and figures are listed without discussion (see also chapter 6).

Table D.1: MSE *and bias of all solutions.*

mission no.	parameters[a]	α	MSE[b]	BNR	max(BSR)[c]
1	1 m, $L = 180$, cn	2.4	11.8	0.2	0.20 (117.9)
2a	6 m, $L = 180$, cn	5.1	2.9	0.06	0.18 (61.4)
2b	6 m, $L = 240$, cn	1.5	12.3	0.4	0.68 (2×10^3)
3	6 m, $L = 180$, wn	5.3	1.5	2.0	0.18 (386.4)
4	SGG+SST, $L = 180$	3.6	0.9	1.2	0.18 (223.0)
5a	SGG+SST/10, $L = 180$	4.3	1	1.6	0.18 (493.0)
5b	SGG+SST/10, $L = 240$	1.4	9.7	0.3	0.66 (3×10^3)
6	SGG+SST/100, $L = 180$	4.9	1.2	1.8	0.18 (539.4)
7a	SGG+Δg, $L = 180$	0.8	1.5	10^{-4}	0.00 (5.7)
7b	SGG+Δg, $L = 240$	1.2	8.5	0.07	0.55 (121.7)
8	SGG+Δg, $L = 180$	1.2	1.5	3×10^{-4}	0.01 (25.1)
9a	SGG+SST/10+Δg, $L = 180$	0.8	0.2	6×10^{-4}	0.00 (5.6)
9b	SGG+SST/10+Δg, $L = 240$	1.2	7.3	0.09	0.55 (121.8)

[a]Except for mission no. 1 with a mission length of 1 month, the mission length is 6 months. The SGG observations are subject to coloured noise with the exception of mission no. 3 where the noise is assumed to be white. The accuracy of the gravity anomalies is $\sigma = 2.5$ mGal, except for mission no. 8 with an accuracy of $\sigma = 5.0$ mGal.

[b]In proportion to mission 5a.

[c]The maximum BSR based on the OSU91A degree-order variances. The maximum BSR between brackets has been computed using the OSU91A coefficients.
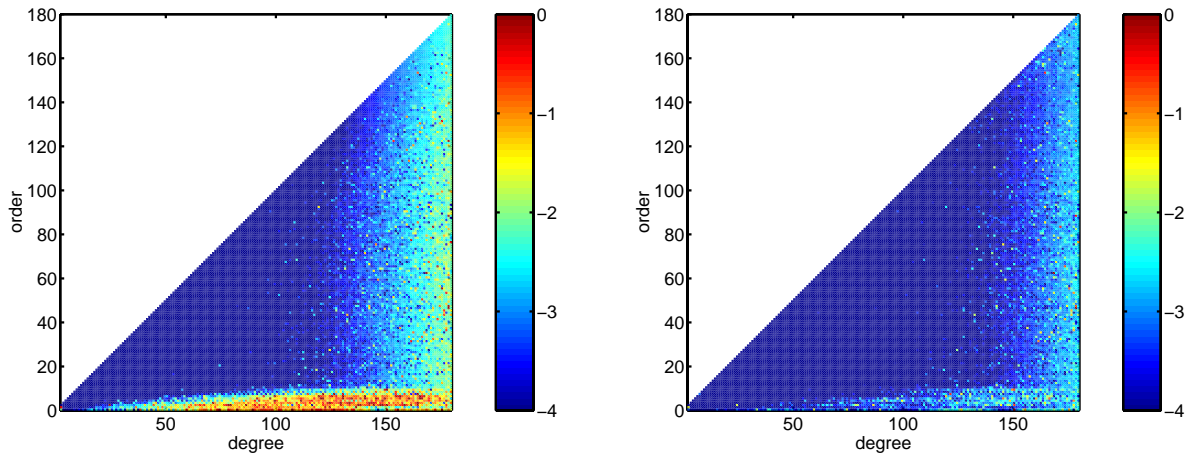
Figure D.1: BSR: SGG *only solution for 6 months, white noise* $L = 180$ *(left) and the combination of* SGG, *6 months, coloured noise and* $\Delta g(\sigma = 5.0 \text{ mGal})$, $L = 180$. *Logarithmic scale.*
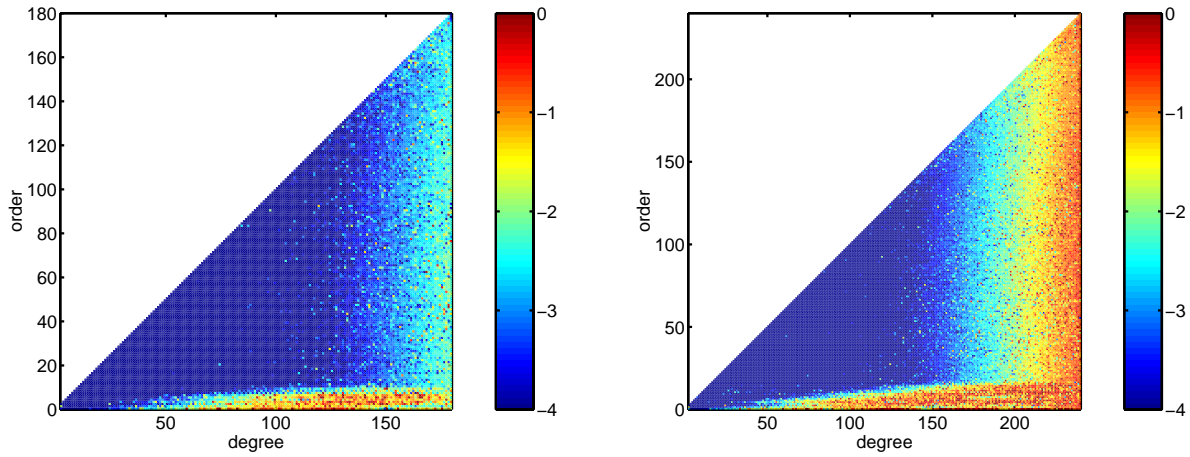

Figure D.2: BSR: *Combination of* SGG *and* SST*/10,* $L = 180$ *(left), and combination of* SGG *and* SST*/10,* $L = 240$ *(right). Logarithmic scale. The combined solutions* SGG + SST *or* SST/100, $L = 180$, *yields figures almost identical to the left panel.*
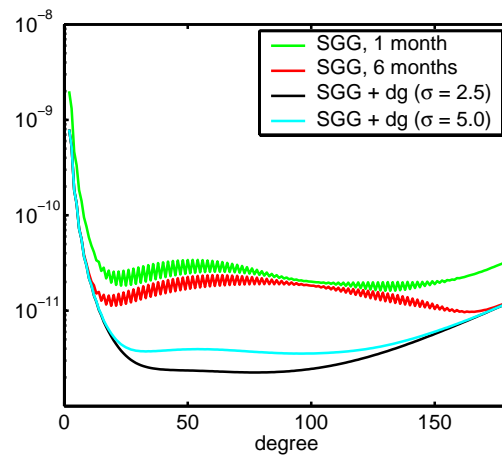

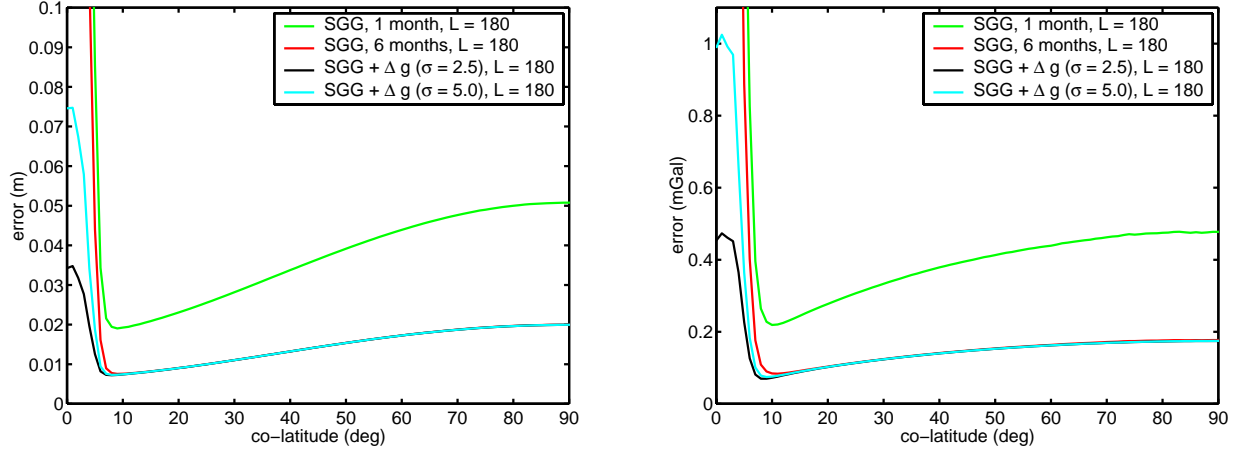Figure D.3: *Error degree variances.*

Figure D.4: MSEM *propagated to geoid heights (left) and gravity anomalies (right).* SGG $+ \Delta g$, $L = 180$.

Table D.2: *Propagated errors for all solutions.*

| mission		geoid height error (cm)				grav. anomaly error (mGal)			
no.	parameters	RMS	mean	max	min	RMS	mean	max	min
1	1 m, $L = 180$, cn	12.3	6.1	70.8	1.9	1.48	0.71	6.98	0.22
2a	6 m, $L = 180$, cn	9.7	3.5	58.8	0.8	1.26	0.43	6.70	0.08
2b	6 m, $L = 240$, cn	11.9	6.2	54.6	1.9	2.23	1.56	10.50	0.63
2b	$l_{max} = 180$	10.8	4.1	59.8	0.9	1.55	0.57	8.66	0.13
3	6 m, $L = 180$, wn	8.3	2.4	47.1	0.3	1.18	0.41	6.73	0.08
4	SGG+SST, $L = 180$	5.9	1.9	32.7	0.3	0.99	0.36	5.71	0.08
5a	SGG+SST/10, $L = 180$	6.5	2.0	37.2	0.3	1.06	0.38	6.02	0.08
5b	SGG+SST/10, $L = 240$	9.0	5.2	41.8	1.8	2.06	1.50	9.47	0.63
5b	$l_{max} = 180$	7.6	2.6	42.1	0.5	1.38	0.51	7.96	0.13
6	SGG+SST/100, $L = 180$	7.0	2.1	38.1	0.4	1.10	0.39	6.47	0.08
7a	SGG+Δg, $L = 180$	1.7	1.5	3.9	0.7	0.18	0.16	0.53	0.07
7b	SGG+Δg, $L = 240$	3.7	3.6	4.6	1.5	1.14	1.11	1.45	0.49
7b	$l_{max} = 180$	1.6	1.5	3.1	0.7	0.17	0.16	0.42	0.08
8	SGG+Δg, $L = 180$	2.1	1.7	7.5	0.7	0.26	0.19	1.03	0.07
9a	SGG+SST/10+Δg, $L = 180$	0.9	0.7	3.2	0.3	0.18	0.16	0.51	0.07
9b	SGG+SST/10+Δg, $L = 240$	3.4	3.3	4.2	1.4	1.14	1.11	1.45	0.49
9b	$l_{max} = 180$	0.8	0.7	2.6	0.3	0.17	0.16	0.41	0.08
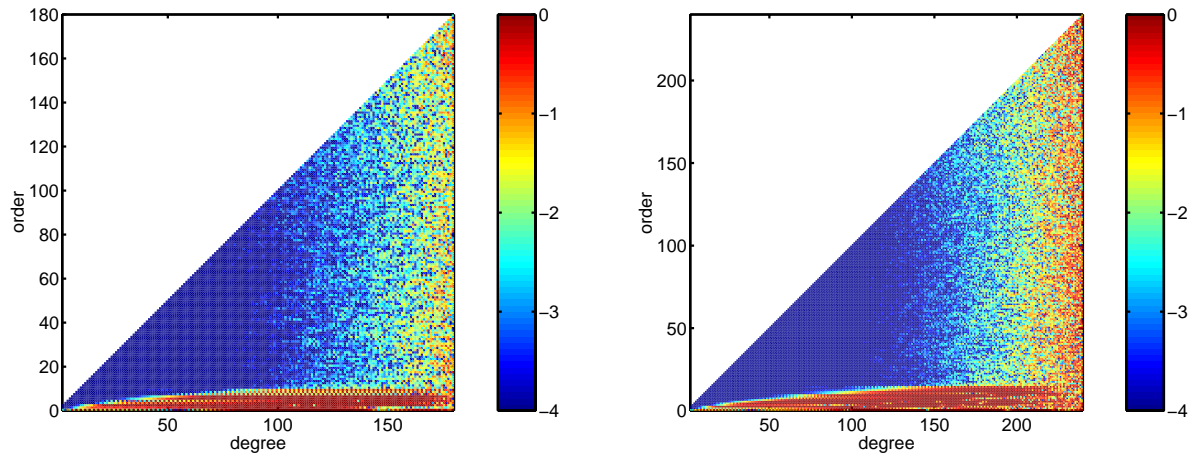
Figure D.5: BNR: SGG, *maximum is* 10^2. *Solution up to degree* $L = 180$ *(left) and* $L = 240$ *(right). The combined solution* SGG $+$ SST$/10$, *yields figures almost identical to the current ones. The maximum* BNR, *however, is* 10^1.
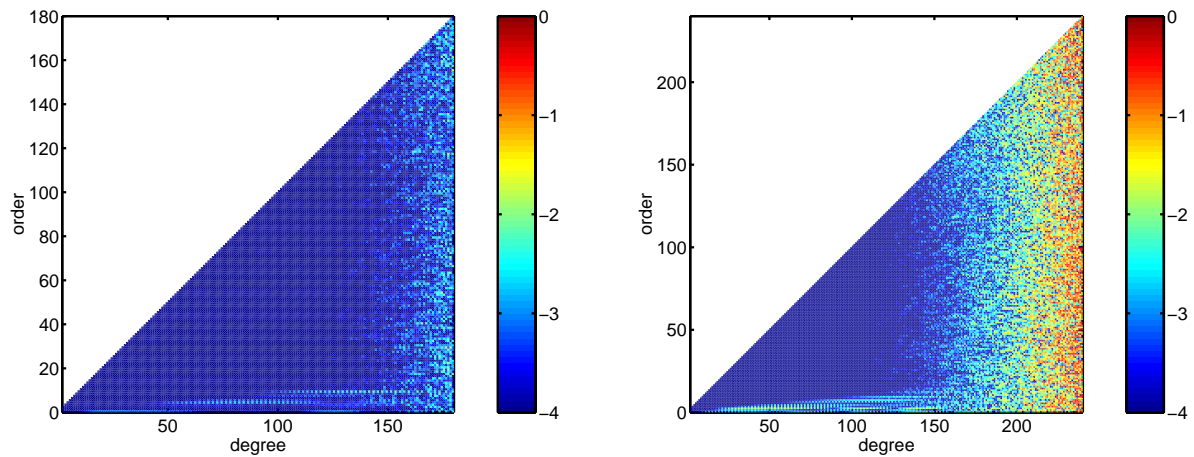

Figure D.6: BNR: SGG $+ \Delta g$, *maxima are* 10^{-2}, *left, and* 10^0, *right. Solution up to degree* $L = 180$ *(left) and* $L = 240$ *(right). The combination of* SGG, SST$/10$ *and* Δg *yields figures identical to the current ones, with the same maximum values.*
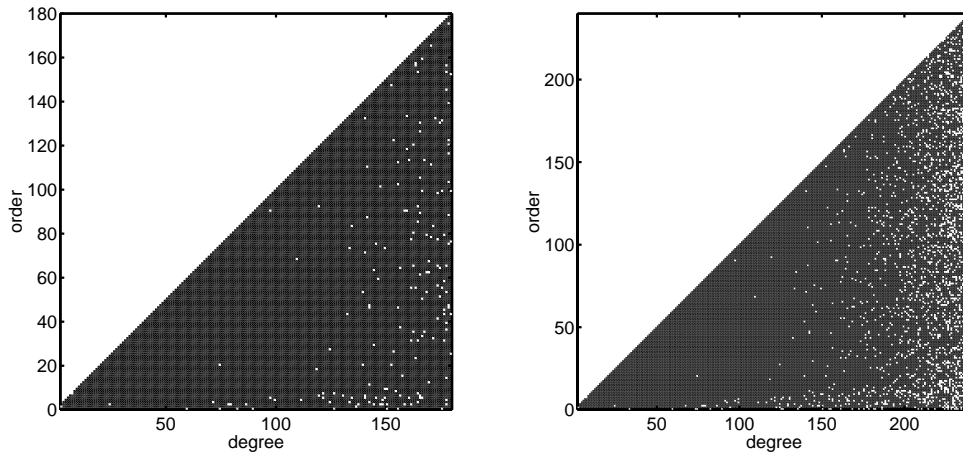
Figure D.7: SNR*: SGG only, maximum is* 10^4. *Solution up to degree* $L = 180$ *(left) and* $L = 240$ *(right).* *The coefficients with an* SNR *larger than or equal to one are shown in black, coefficients with an* SNR *smaller than one are shown in white. The combination of* SGG *and* SST/10 *yields figures identical to the current ones. The maximum* SNR*, however, is* 10^6.

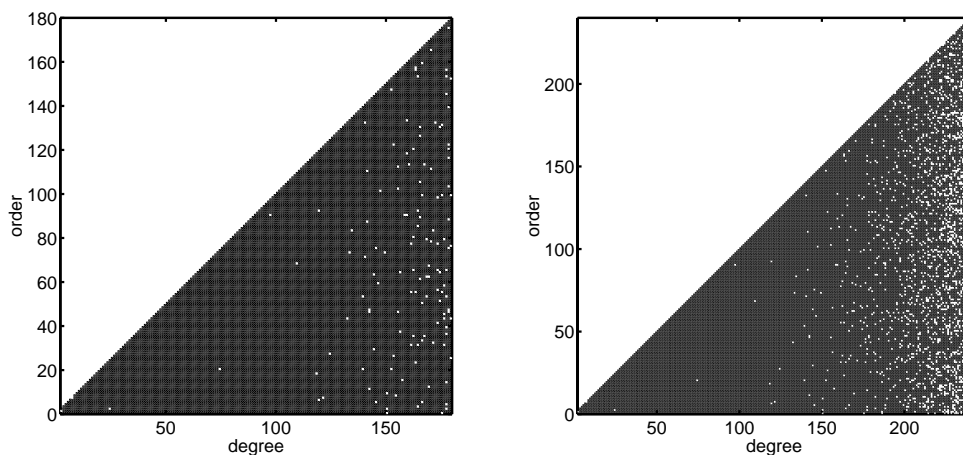Figure D.8: SNR*: SGG +* Δg, *maximum is* 10^4. *Solution up to degree* $L = 180$ *(left) and* $L = 240$ *(right). The coefficients with an* SNR *larger than or equal to one are shown in black, coefficients with an* SNR *smaller than one are shown in white. The combination of* SGG*,* SST/10 *and* Δg *yields figures identical to the current ones. The maximum* SNR*, however, is* 10^6.

References

Backus, G. and Gilbert, J. (1967). Numerical applications of a formalism for geophysical inverse problems. *Geophys. J. R. astr. Soc.*, **13**, 247–276.

Backus, G. and Gilbert, J. (1968). The resolving power of gross earth data. *Geophys. J. R. astr. Soc.*, **16**, 169–205.

Balmino, G., Schrama, E., and Sneeuw, N. (1996). Compatibility of first-order circular orbit perturbations theories; consequences for cross-track inclination functions. *Journal of Geodesy*, **70**, 554–561.

Barriot, J., Valés, N., Balmino, G., and Rosenblatt, P. (1998). A 180th degree and order model of the Venus gravity field from Magellan line of sight residual Doppler data. *Geophysical Research Letters*, **25**(19), 3743–3746.

Blatter, C. (1998). *Wavelets, a primer*. A K Peters.

Bouman, J. (1993). *The normal matrix in gravity field determination with satellite methods; its stabilization, its information content and its use in error propagation*. Master's thesis, Faculty of Geodetic Engineering, Delft University of Technology.

Bouman, J. (1998a). Quality assessment of geopotential models by means of redundancy decomposition? *DEOS Progress Letter*, **98.2**, 81–89.

Bouman, J. (1998b). Quality of regularization methods. DEOS Report no 98.2, Delft Institute for Earth-Oriented Space Research.

Bouman, J. (1998c). A survey of global gravity models. DEOS Report no 98.3, Delft Institute for Earth-Oriented Space Research.

Bouman, J. and Koop, R. (1998a). Quality differences between Tikhonov regularization and generalized biased estimation in gradiometric analysis. *DEOS Progress Letter*, **98.2**, 69–80.

Bouman, J. and Koop, R. (1998b). Regularization in gradiometric analysis. *Physics and Chemistry of the Earth*, **23**(1), 41–46.

Bouman, J. and Koop, R. (1998c). Stabilization of global gravity field solutions by combining satellite gradiometry and airborne gravimetry. *DEOS Progress Letter*, **98.1**, 43–55.

Bouman, J. and Koop, R. (1999). Quality of global gravity field solutions from SST and SGG. Presented at the EGS XXIV General Assembly, The Hague. Submitted to *Journal of Geodynamics*.

Chovitz, B. (1988). Parameters of common relevance of astronomy, geodesy, and geodynamics. *Bulletin Géodésique*, **62**(3), 359–367.

Colombo, O. (1981). Numerical methods for harmonic analysis on a sphere. Report No. 310, Department of Geodetic Science and Surveying, Ohio State University.

Davis, G. (1997). Exploring the limits of GPS-based precise orbit determination. *Navigation*, **44**(2), 181–193.

Eddy, W., McCarthy, J., Pavlis, D., Marshall, J., Luthke, S., Tsaoussi, L., Leung, G., and Williams, D. (1990). GEODYN-II system operation manual. Contractor report Vol. 1-5, STX System Corp.

Eldén, L. (1982). A weighted pseudoinverse, generalized singular values, and constrained least squares problems. *BIT*, **22**, 487–502.

Engl, H. (1997). *Integralgleichungen*. Springer, Wien, New York.

Engl, H., Hanke, M., and Neubauer, A. (1996). *Regularization of Inverse Problems*. Kluwer Academic Publishers.

ESA (1999). Gravity Field and Steady-State Ocean Circulation Mission. Reports for mission selection; the four candidate earth explorer core missions. ESA SP-1233(1).

Floberghagen, R. and Bouman, J. (1998). On the information content and regularisation of lunar gravity field solutions. *DEOS Progress Letter*, **98.1**, 1–19.

Freeden, W. and Schneider, F. (1998). Regularization wavelets and multiresolution. *Inverse problems*, **14**, 225–243.

Gelderen, M. van (1992). The geodetic boundary value problem in two dimensions and its iterative solution. Publications on geodesy. New series no. 35, Netherlands Geodetic Commission.

Gelderen, M. van (1998). Error propagation for satellite gradiometry. *DEOS Progress Letter*, **98.2**, 57–68.

Gelderen, M. van and Koop, R. (1997). The use of degree variances in satellite gradiometry. *Journal of Geodesy*, **71**, 337–343.

Golub, G. and van Loan, C. (1996). *Matrix computations*. The Johns Hopkins University Press, third edition.

Golub, G., Heath, M., and Wahba, G. (1979). Generalized cross-validation as a method for choosing a good ridge parameter. *Technometrics*, **21**(2), 215–223.

Groetsch, C. (1980). *Elements of applicable functional analysis*. Marcel Dekker.

Groetsch, C. (1984). *The theory of Tikhonov regularization for Fredholm integral equations of the first kind*. Pitman.

Groetsch, C. (1993). *Inverse problems in the mathematical sciences*. Vieweg, Wiesbaden.

Gruber, T., Anzenhofer, M., and Rentsch, M. (1995). The 1995 GFZ high resolution gravity model. In R. Rapp, A. Cazenave, and R. Nerem, editors, *IAG Symposia 116 - Global gravity field and its temporal variations*. Springer, Berlin.

Haagmans, R. and van Gelderen, M. (1991). Error variances-covariances of GEM-T1: their characteristics and implications in geoid computation. *Journal of Geophysical Research*, **96**(B12), 20011–20022.

Hansen, P. (1990). The discrete Picard condition for discrete ill-posed problems. *BIT*, **30**, 658–672.

Hansen, P. (1992). Analysis of discrete ill-posed problems by means of the L-curve. *SIAM Review*, **34**(4), 561–580.

Hansen, P. (1997). *Regularization Tools, A Matlab package for analysis and solution of discrete ill-posed problems, Version 2.1 for Matlab 5.0.* Department of Mathematical Modelling, Technical University of Denmark. http://www.imm.dtu.dk/~pch.

Hansen, P. (1999). The L-curve and its use in the numerical treatment of inverse problems. In P. Johnston, editor, *Inverse problems in electrocardiology*, volume 3 of *Advances in computational biomedicine*. WIT Press. to appear.

Hansen, P. and O'Leary, D. (1993). The use of the L-curve in the regularization of discrete ill-posed problems. *SIAM J. Sci. Comput.*, **14**(6), 1487–1503.

Heck, B. (1990). An evaluation of some systematic error sources affecting terrestrial gravity anomalies. *Bulletin Géodésique*, **64**, 88–108.

Heiskanen, W. and Moritz, H. (1967). *Physical geodesy*. W.H. Freeman and Co.

Hemmerle, W. (1975). An explicit solution for generalized ridge regression. *Technometrics*, **17**, 309–314.

Hemmerle, W. and Brantle, T. (1978). Explicit and constrained generalized ridge estimation. *Technometrics*, **20**(2), 109–120.

Hoerl, A. and Kennard, R. (1970). Ridge regression: biased estimation for nonorthogonal problems. *Technometrics*, **12**(1), 55–67.

Hotine, M. (1967). Downward continuation of the gravitational potential. In M. H. (1991), editor, *Differential geodesy*, pages 143–148. Springer, Berlin.

Ilk, K. (1986). On the regularization of ill-posed problems. Proc. Int. Symp. Figure and Dynamics of the Earth, Moon, and Planets. Prague.

Ilk, K. (1993). Regularization for high resolution gravity field recovery by future satellite techniques. In G. Anger, R. Gorenflo, H. Jochmann, H. Moritz, and W. Webers, editors, *Inverse problems: principles and applications in geophysics, technology, and medicine*, volume 74 of *Mathematical Research*. Akademie, Berlin. Proceedings of the International Conference held in Potsdam, August 30 - September 3, 1993.

Ivanov, V. (1962). Integral equations of the first kind and an approximate solution for the inverse problem of potential. *Soviet Math. Doklady*, **3**, 210–212.

Jekeli, C. (1978). An investigation of two models for the degree variances of global covariance functions. Report No. 275, Department of Geodetic Science and Surveying, Ohio State University.

Kaula, W. (1966). *Theory of satellite geodesy*. Blaisdell Pub. Co.

Klees, R. (1999). Numerical analysis. Lecture notes, Department of Geodetic Engineering, Faculty of Civil Engineering and Geosciences, Delft University of Technology, Delft.

Klees, R., Koop, R., Visser, P., and van den IJssel, J. (1999). Fast gravity field recovery from GOCE gravity gradient observations. Delft Institute for Earth-Oriented Space Research (DEOS), Delft University of Technology. Submitted to *Journal of Geodesy*.

Konopliv, A. and Sjogren, W. (1995). *The JPL Mars gravity field, Mars50c, based upon Viking and Mariner 9 Doppler tracking data*. JPL Publication 95-5. Jet Propulsion Laboratory, Pasadena, California.

Konopliv, A. and Sjogren, W. (1996). *Venus Gravity Handbook*. JPL Publication 96-2. Jet Propulsion Laboratory, Pasadena, California.

Konopliv, A., Binder, A., Hood, L., Kucinskas, A., Sjogren, W., and Williams, J. (1998). Improved Gravity Field of the Moon from Lunar Prospector. *Science Magazine*, **281**, 1476–1480.

Koop, R. (1993). Global gravity field modelling using satellite gravity gradiometry. Publications on geodesy. New series no. 38, Netherlands Geodetic Commission.

Kress, R. (1989). *Linear integral equations*. Springer, Berlin.

Kreyszig, E. (1989). *Introductory functional analysis with applications*. John Wiley and Sons.

Lanczos, C. (1961). *Linear differential operators*. Van Nostrand Company Ltd.

Lawson, C. and Hanson, R. (1974). *Solving least squares problems*. Prentice-Hall.

Lemoine, F., Smith, D., Zuber, M., Neumann, G., and Rowlands, D. (1997). A 70th degree lunar gravity model (GLGM-2) from Clementine and other tracking data. *Journal of Geophysical Research*, **102**(E7), 16339–16359.

Lemoine, F., Smith, D., Kunz, L., Smith, R., Pavlis, E., Pavlis, N., Klosko, S., Chinn, D., Torrence, M., Williamson, R., Cox, C., Rachlin, K., Wang, Y., Kenyon, S., Salman, R., Trimmer, R., Rapp, R., and Nerem, R. (1999). The development of the NASA GSFC and NIMA joint geopotential model. In J. Segawa, H. Fujimoto, and S. Okubo, editors, *IAG Symposia 117 - Gravity, geoid and marine geodesy*, pages 461–469. Springer, Berlin.

Louis, A. (1989). *Inverse und schlecht gestellte Probleme*. Teubner.

Marsh, J., Lerch, F., Putney, B., Christodoulidis, D., Smith, D., Felsentreger, T., Sanchez, B., Klosko, S., Pavlis, E., Martin, T., Williamson, J. R. R., Colombo, O., Rowlands, D., Eddy, W., Chandler, N., Rachlin, K., Patel, G., Bhati, S., and Chinn, D. (1988). A new gravitational model for the earth from satellite tracking data: GEM-T1. *Journal of Geophysical Research*, **93**(B6), 6169–6215.

Moritz, H. (1980). Geodetic reference system 1980. *Bulletin Géodésique*, **54**, 395–405.

Morozov, V. (1984). *Methods for solving incorrectly posed problems*. Springer, New York, Berlin, Heidelberg.

Nashed, M. (1976). Aspects of generalized inverses in analysis and regularization. In M. Nashed, editor, *Generalized inverses and applications*, pages 193–244.

Nerem, R., Bills, B., and McNamee, J. (1993). A high resolution gravity model for Venus: GVM-1. *Geophysical Research Letters*, **20**(7), 599–602.

Nerem, R., Lerch, F., Marshall, J., Pavlis, E., Putney, B., Tapley, B., Eanes, R., Ries, J., Schutz, B., Shum, C., Watkins, M., Klosko, S., Chan, J., Luthcke, S., Patel, G., Pavlis, N., Williamson, R., Rapp, R., Biancale, R., and Nouel, F. (1994). Gravity model development for Topex/Poseidon: Joint Gravity Models 1 and 2. *Journal of Geophysical Research*, **99**(C12), 24421–24447.

Neyman, Y. (1985). Improperly posed problems in geodesy and methods of their solution. In K. Schwarz, editor, *Local Gravity Field Approximation*, pages 499–566.

Oppenheim, A., Willsky, A., and Young, I. (1983). *Signals and Systems*. Prentice-Hall.

Overhauser, A. (1968). Analytic definition of curves and surfaces by parabolic blending. Techn. Report No. SL68-40, Scientific Research Staff Publication, Ford Motor Company, Detroit.

Parker, R. (1994). *Geophysical inverse theory*. Princeton University Press.

Phillips, D. (1962). A technique for the numerical solution of certain integral equations of the first kind. *Journal of the Association for Computing Machinery*, **9**, 84–97.

Press, W., Teukolsky, S., Vetterling, W., and Flannery, B. (1992). *Numerical recipes in C: the art of scientific computing*. Cambridge University Press, second edition.

Rapp, R. (1972). Geopotential coefficient behavior to high degree and geoid information by wavelength. Report No. 180, Department of Geodetic Science and Surveying, Ohio State University.

Rapp, R. (1979). Potential coefficient and anomaly degree variance modelling revisited. Report No. 293, Department of Geodetic Science and Surveying, Ohio State University.

Rapp, R., Wang, Y., and Pavlis, N. (1991). The Ohio State 1991 geopotential and sea surface topography harmonic coefficient models. Report No. 410, Department of Geodetic Science and Surveying, Ohio State University.

Rauhut, A. (1992). *Regularization methods for the solution of the inverse Stokes problem*. Ph.D. thesis, The University of Calgary.

Regińska, T. (1996). A regularization parameter in discrete ill-posed problems. *SIAM J. Sci. Comput.*, **17**(3), 740–749.

Reigber, C. (1989). Gravity field recovery from satellite tracking data. In F. Sansò and R. Rummel, editors, *Theory of satellite geodesy and gravity field determination*, pages 197–234. Springer, Berlin.

Ries, J., Eanes, R., Shum, C., and Watkins, M. (1992). Progress in the determination of the gravitational coefficient of the earth. *Geophysical Research Letters*, **19**(6), 529–531.

Rummel, R. (1986). Satellite gradiometry. In H. Sünkel, editor, *Mathematical and numerical techniques in physical geodesy*, volume 7 of *Lecture notes in earth sciences*, pages 318–363. Springer, Berlin.

Rummel, R. (1988). Inertial surveying. Lecture notes, Faculty of Geodetic Engineering, Delft University of Technology, Delft.

Rummel, R., Schwarz, K., and Gerstl, M. (1979). Least squares collocation and regularization. *Bulletin Géodésique*, **53**, 343–361.

Rummel, R., van Gelderen, M., Koop, R., Schrama, E., Sansò, F., Brovelli, M., Miggliaccio, F., and Sacerdote, F. (1993). Spherical harmonic analysis of satellite gradiometry. Publications on geodesy. New series no. 39, Netherlands Geodetic Commission.

Schneider, F. (1997). *Inverse problems in satellite geodesy and their approximate solution by splines and wavelets*. Ph.D. thesis, Universität Kaiserslautern.

Schrama, E. (1989). The role of orbit errors in processing of satellite altimeter data. Publications on geodesy. New series no. 33, Netherlands Geodetic Commission.

Schrama, E. (1990). Gravity field error analysis: application of GPS receivers and gradiometers on low orbiting platforms. TM 100769, NASA.

Schrama, E. (1991). Gravity fiels error analysis: Application of GPS receivers and gradiometers on low orbiting platforms. *Journal of Geophysical Research*, **96**(B12), 20041–20051.

Schreiner, M. (1994). *Tensor spherical harmonics and their application in satellite gradiometry*. Ph.D. thesis, Universität Kaiserslautern.

Schuh, W. (1996). Tailored numerical solution strategies for the global determination of the earth's gravity field. Folge 81, Mitteilungen der geodätischen Institute der Technischen Universität Graz.

Schuh, W. (1999). Scientific data processing algorithms. in: ESA, From Eötvös to milligal, midterm report, WP 3.

Schwarz, K. (1979). Geodetic improperly posed problems and their regularization. *Bollettino di Geodesia e Scienze Affini*, **38**(3), 389–416.

Schwarz, K. and Li, Z. (1997). An introduction to airborne gravimetry and its boundary value problems. In F. Sansò and R. Rummel, editors, *Geodetic Boundary Value Problems in View of the One Centimeter Geoid*, volume 65 of *Lecture notes in earth sciences*, pages 312–358. Springer, Berlin.

Schwintzer, P. (1990). Sensitivity analysis in least squares gravity field modelling by means of redundancy decomposition of stochastic a priori information. Deutsches Geodätiches Forschungsinstitut. Internal report.

Schwintzer, P., Reigber, C., Bode, A., Kang, Z., Zhu, S., Massmann, F., Raimondo, J., Biancale, R., Balmino, G., Lemoine, J., Moynot, B., Marty, J., Barlier, F., and Boudon, Y. (1997). Long-wavelength global gravity field models: GRIM4-S4, GRIM4-C4. *Journal of Geodesy*, **71**, 189–208.

Sneeuw, N. (1991). Inclination functions, group theoretical background and a recursive algorithm. 91.2, Reports of the Faculty of Geodetic Engineering.

Strang, G. (1986). *Introduction to applied mathematics*. Wellesley-Cambridge press.

Tapley, B. (1996). Gravity recovery and climate experiment (GRACE); Proposal to NASA's earth system science pathfinder program. , CSR.

Teunissen, P. (1994). Mathematische geodesie I, inleiding vereffeningstheorie. Lecture notes, Faculty of Geodetic Engineering, Delft University of Technology, Delft.

Teunissen, P. (1995). Mathematische geodesie II, inleiding toetsingstheorie. Lecture notes, Faculty of Geodetic Engineering, Delft University of Technology, Delft.

Teunissen, P. (1996). Navigatie I, inleiding filtertheorie. Lecture notes, Faculty of Geodetic Engineering, Delft University of Technology, Delft.

Thalhammer, M. (1995). Regionale Gravitationsfeldbestimmung mit zukünftigen Satellitenmissionen (SST und Gradiometry). Reihe C No. 437, Deutsche Geodätische Kommission.

Tiberius, C. (1998). Recursive data processing for kinematic GPS surveying. Publications on geodesy. New series no. 45, Netherlands Geodetic Commission.

Tikhonov, A. (1963a). Regularization of incorrectly posed problems. *Soviet Math. Dokl.*, **4**, 1624–1627.

Tikhonov, A. (1963b). Solution of incorrectly formulated problems and the regularization method. *Soviet Math. Dokl.*, **4**, 1035–1038.

Tikhonov, A. and Arsenin, V. (1977). *Solutions of ill-posed problems*. Winston and Sons.

Trampert, J. and Snieder, R. (1996). Model estimations biased by truncated expansions: possible artifacts in seismic tomography. *Science*, **271**, 1257–1260.

Tscherning, C. and Rapp, R. (1974). Closed covariance expressions for gravity anomalies, geoid undulations, and deflections of the vertical implied by anomaly degree variance models. Report No. 208, Department of Geodetic Science and Surveying, Ohio State University.

Varga, R. (1962). *Matrix iterative analysis*. Prentice-Hall.

Vinod, H. and Ullah, A. (1981). *Recent advances in regression methods*. Marcel Dekker.

Visser, P., Wakker, K., and Ambrosius, B. (1994). Global gravity field recovery from the ARISTOTE-LES satellite mission. *Journal of Geophysical Research*, **99**(B2), 2841–2851.

Visser, P., van den IJssel, J., and Koop, R. (2000). WP 340: simulation of GOCE orbit determination with GPS. In *SID: GOCE end to end performance analysis, final report*. ESTEC contract no. 12735/98/NL/GD.

Vogel, C. (1996). Non-convergence of the L-curve regularization parameter selection method. *Inverse Problems*, **12**, 535–547.

Wahba, G. (1990). *Spline models for observational data*. SIAM.

Wing, G. (1991). *A primer on integral equations of the first kind: the problem of deconvolution and unfolding*. SIAM.

Xu, P. (1992a). Determination of surface gravity anomalies using gradiometric observables. *Geophysical Journal International*, **110**, 321–332.

Xu, P. (1992b). The value of minimum norm estimation of geopotential fields. *Geophysical Journal International*, **111**, 170–178.

Xu, P. (1998). Truncated SVD methods for discrete linear ill-posed problems. *Geophysical Journal International*, **135**, 505–514.

Xu, P. and Rummel, R. (1994a). Generalized ridge regression with applications in determination of potential fields. *Manuscripta Geodetica*, **20**, 8–20.

Xu, P. and Rummel, R. (1994b). A simulation study of smoothness methods in recovery of regional gravity fields. *Geophysical Journal International*, **117**, 472–486.

IJssel, J. van den, Koop, R., and Visser, P. (2000). WP 640: Level $1 \rightarrow 2$ simplified deterministic retrieval. In *SID: GOCE end to end performance analysis, final report*. ESTEC contract no. 12735/98/NL/GD.

Curriculum Vitae

8-3-1969	Geboren te Middelburg
1987	Eindexamen VWO aan de C.S.G. Blaise Pascal te Spijkenisse
1993	Doctoraalexamen geodetisch ingenieur aan de Technische Universiteit Delft
1993-1994	Toegevoegd onderzoeker bij de sectie Fysische-, Meetkundige- en Ruimtegeodesie aan de Faculteit der Geodesie van de Technische Universiteit Delft
1994-1999	Assistent in opleiding (AiO) bij de sectie Fysische-, Meetkundige- en Ruimtegeodesie aan de Faculteit der Geodesie van de Technische Universiteit Delft